Nanoscale Forces and Their Uses in Self-Assembly

*Kyle J. M. Bishop, Christopher E. Wilmer, Siowling Soh, and Bartosz A. Grzybowski**

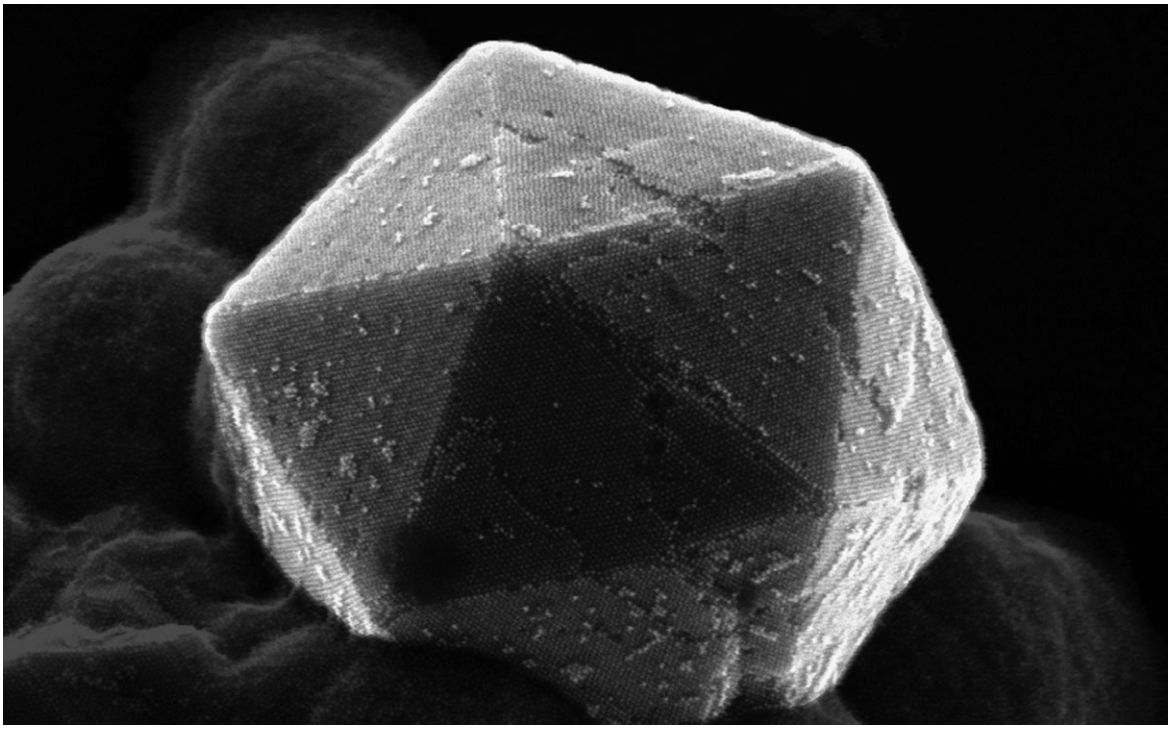

From the Contents

The ability to assemble nanoscopic components into larger structures and materials depends crucially on the ability to understand in quantitative detail and subsequently "engineer" the interparticle interactions. This Review provides a critical examination of the various interparticle forces (van der Waals, electrostatic, magnetic, molecular, and entropic) that can be used in nanoscale self-assembly. For each type of interaction, the magnitude and the length scale are discussed, as well as the scaling with particle size and interparticle distance. In all cases, the discussion emphasizes characteristics unique to the nanoscale. These theoretical considerations are accompanied by examples of recent experimental systems, in which specific interaction types were used to drive nanoscopic self-assembly. Overall, this Review aims to provide a comprehensive yet easily accessible resource of nanoscale-specific interparticle forces that can be implemented in models or simulations of self-assembly processes at this scale.

Frontispiece image courtesy of R. Klajn.

NANO MICRO small

1. Introduction

The focus of nanoscience and nanotechnology is gradually shifting from the synthesis of individual components to their assembly into larger systems and nanostructured materials. After over two decades of intense research, there are now hundreds if not thousands of procedures available that allow for crafting the sizes, shapes, material properties, or surface chemistries of nanoscopic particles. Nanoscopic spheres,[1] Platonic polyhedra,[2,3] rods,[2–5] ellipsoids,[6] plates,[7–10] tripdods or tetrapods,[11,12] core/shell[13,14] and voided core/shell particles,[15,16] nanocages,[17–19] and dumbbells[20–22] can be made in large quantities with ever improving monodispersity (Figure 1). Nanosynthetic methods are applicable to a range of metals,[13,23–26] semiconductors,[27,28] oxides,[29,30] inorganic salts,[31,32] and polymers.[33,34] These nanoparticulate materials can be functionalized flexibly using organic ligands terminated in functionalities imparting desired surface properties: solubility in selected solvents, specificity towards small molecules or larger biologicals,[35–37] resistance to nonspecific adsorption,[38] net electric charge,[39–41] electrochemical activity,[42–45] and more.

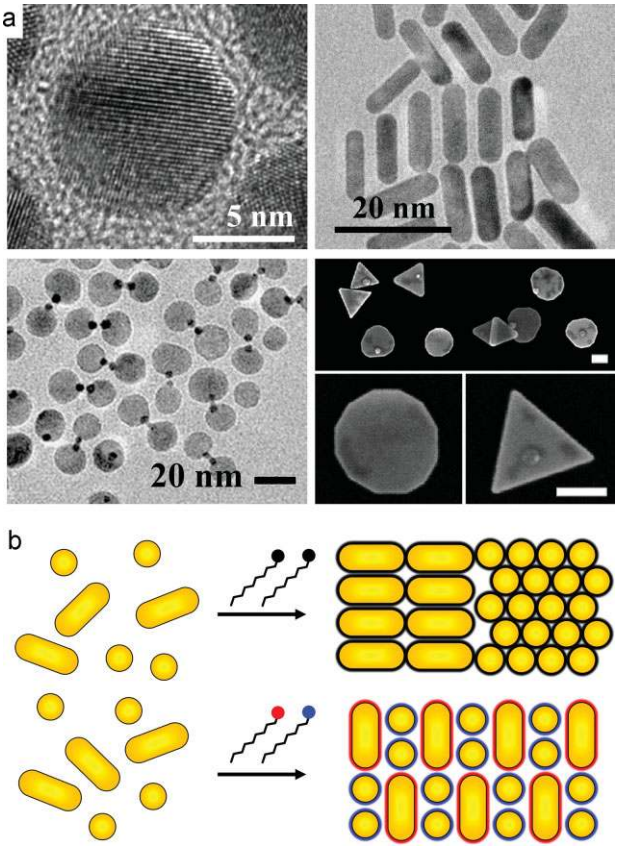

Figure 1. a) The variety of nanoscale particles. Clockwise from top left: a single gold nanoparticle illustrating the underlying atomic structure (image courtesy of R. Klajn); gold nanorods capped with CTAB ligands (image courtesy of D. A. Walker); plate-like gold prisms ≈10 nm in thickness (scale bar = 100 nm). Reprinted from Reference [7]. Two-domain Au/Fe_3O_4 (Au domains are smaller and darker) nanoparticles crosslinked to form dimeric superstructures (image courtesy of Y. Wei). b) Schematic illustration of nanoscale self-assembly. In addition to "body" forces between the material particles (e.g., vdW or magnetic interactions), the interactions between nanoscale spheres and rods can be tuned controllably through appropriate surface functionalization. For different interparticle interaction potentials, the particles organize into qualitatively different structures. Here, vdW attraction (Section 2) and steric repulsion (Section 7) induce the phase separation of rods and spheres into two close-packed arrangements (top). Alternatively, when the rods are functionalized with positively charged ligands and the spheres with negatively charge ligands (Section 4), the particles are expected to organize via electrostatic interactions into a binary lattice.

Despite this enormous progress, however, nanoscience is currently in a somewhat precarious position. Heralded as the "next technological revolution" (after the steam engine, electricity, and information technology), it has been fueled by a constant and generous stream of funding that is globally estimated at around $12.4 bn per year.[46] To realize these great expectations, nanoscience must now deliver truly revolutionary solutions for medical diagnostics,[47–49] drug delivery,[50,51] sensors,[52] electronic devices,[53,54] or new materials of unique properties.[55] Importantly, many of these applications are based not on individual nano-objects but rather on assemblies in which these nano-objects interact with one another and organize in purposeful ways. Thus, the challenge that is facing nanoscience is to develop efficient and robust ways of assembling nanocomponents.

Self-assembly (SA)[56,57] is arguably the most promising candidate for this task as it can, at least in principle, evolve large numbers of individual particles of appropriately chosen properties into higher-order structures (Figure 1b). There are several outstanding examples of successful application of SA at the nanoscale: from systems serving as ultrasensitive biosensors,[58] through highly conductive nanowires of uniform-width,[59] ordered two-dimensional (2D) nanoparticle arrays exhibiting unique electronic properties,[32,60–62] to materials of overall macroscopic dimensions and exhibiting unusual bulk properties (e.g., plastic metals[63]). These and other demonstrations of nanoscale SA (nSA) depend crucially on our ability to understand and "engineer" the interactions between nanoscopic particles and to evolve them into a desired structure(s). Without this ability, no rational design of nSA is possible, and the quest for tailored nanomaterials appears somewhat hopeless.

Since the fundamental interactions between atoms/molecules and between colloids (i.e., particles of sizes above ~100 nm[64]) are by now well understood, extrapolating this knowledge to the "intermediate" nanoscale regime should be straightforward, and the expressions/formulas with which to model nanoscopic forces should be easily accessible. Unfortunately, this is not the necessarily case. The prevalent approach – also in many of our own previous works – to nanoscopic forces has been to use formulas derived previously for colloids[65–67] and only change the dimensions of the interacting particles.

[*] K. J. M. Bishop, C. E. Wilmer, S. Soh, Prof. B. A. Grzybowski
Department of Chemical and Biological Engineering
Department of Chemistry
Northwestern University
2145 Sheridan Rd, Tech E136
Evasnton, IL 60208 (USA)
E-mail: grzybor@northwestern.edu

Supporting Information is available on the WWW under http://www.small-journal.com or from the author.

DOI: 10.1002/smll.200900358

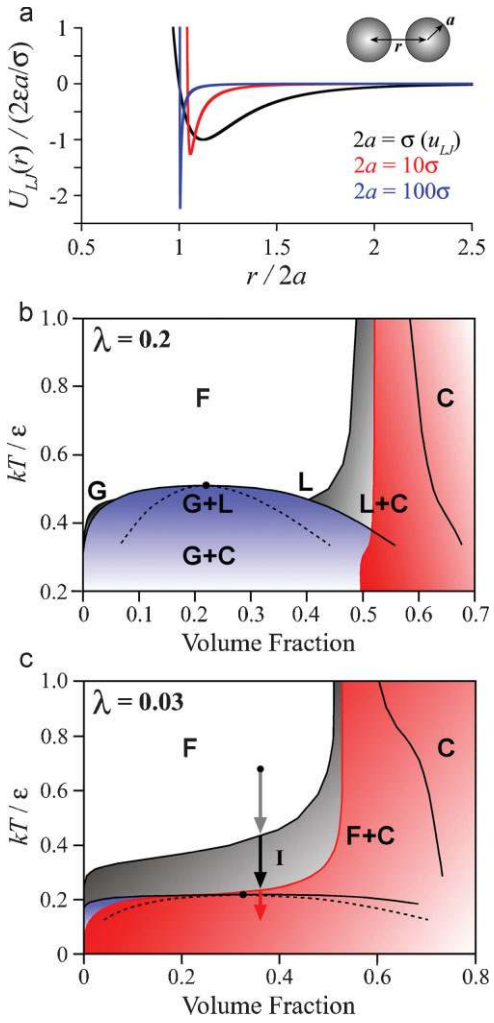

Figure 2. a) A prototypical colloidal potential, $U_{LJ}(r)$, derived by integrating the atomic Lennard–Jones interactions over the volume of the two spheres (cf. Equation (2) for an approximate form valid at small separations and Reference [68] for a detailed derivation). Plots are presented in dimensionless form whereby energy is measured in units of $2\varepsilon a/\sigma$ and distance in units of particle diameter, $2a$. b,c) Phase diagrams adapted from References [74,75] for hard-sphere particles interacting by attractive Yukawa potentials (Equation (5)) with a length scale λ. The solid black curves denote the phase boundaries between fluid (F), gas (G), liquid (L), and crystal (C) phases; the dashed curve is the spinodal. The gray and blue areas denote regions of fluid–solid and gas–liquid coexistence (note that the gas and liquid phases become metastable below the fluid–solid phase boundary). The red curve denotes the dynamical arrest curve, calculated by mode coupling theory (MCT)[74,75,276] and separating the ergodic equilibrium phases from the non-ergodic dynamically arrested states (e.g., gels and glasses). See Reference [74] and references therein for more information.

While this strategy might work in some cases, there is precious little literature[67] to justify it and to prove/disprove its applicability at the nanoscale. Therefore, the present Review aims to re-examine critically the characteristics of various types of interparticle interactions (van der Waals, electrostatic, magnetic, molecular, and entropic) at the nanoscale. For each type, we wish to determine the magnitude and the length scale of the interaction, as well as its scaling with particle size and interparticle distance. The overriding goals of these analyses are then to establish: i) What effects or behaviors emerge that are unique to the nanoscale (as compared to smaller molecular systems or larger colloids); ii) which theoretical tools can be used to model the interactions at various levels of approximation, and iii) what are the limits of any approximate forms. These theoretical considerations are accompanied by examples of recent experimental systems, in which specific interaction types were used to drive nanoscopic self-assembly. Overall, it is our hope that this Review will provide a resource – easily accessible to a general nanoscience audience – of nanoscale-specific interparticle potentials that can be implemented in models or simulations of self-assembly processes at this scale.

Bartosz A. Grzybowski graduated summa cum laude in chemistry from Yale University in 1995. He obtained his doctoral degree in physical chemistry from Harvard University in August 2000 (with G. M. Whitesides). In June 2003 he joined the faculty of Northwestern University, where he is now an associate professor of chemistry and chemical and biological engineering. His scientific interests include self-assembly in non-equilibrium/dynamic systems, complex chemical networks, nanostructured materials, and nanobiology. He is a recipient of the NSF CAREER, the American Chemical Society Unilever, and the Gerhard Kanig Innovation Award, and has recently been named a Pew Scholar in the Biomedical Sciences, Alfred P. Sloan Fellow, and Dreyfus Teacher-Scholar. His first book, "Chemistry in Motion" on micro- and nanoscale reaction diffusion systems has just been published by Wiley.

2. General Aspects of Interaction Magnitudes and Length Scales

Before examining the specific types of interactions useful for nanoscale self-assembly, it is instructive to address some general questions regarding the "generic" characteristics of arbitrary interaction potentials. For example, how strong should the interparticle interactions be to induce self-assembly from solution? Can they be too strong as to prevent the formation of an ordered, equilibrium structure? What is the role of the interaction length scale in the assembly process? As we discuss in this section, the ability of a given interaction potential to induce self-assembly depends on both its magnitude and length scale. Furthermore, the range of an interaction relative to the sizes of interacting particles can determine whether or not these particles will assemble into an ordered structure or into an amorphous phase (Section 2.3).

2.1. Common Scalings of Interaction Length and Strength

Interactions between nanoscale components differ substantially from the molecular interactions from which they derive. Consider the ubiquitous Lennard–Jones (LJ) potential used to approximate the interaction potential between spherical atoms (e.g., argon) and accounting for both

NANO MICRO small

attractive van der Waals (vdW) forces and repulsive exchange interactions due to overlap of electron orbitals (Figure 2a, black curve).

$$u_{LJ}(r) = 4\varepsilon\left[\left(\frac{\sigma}{r}\right)^{12} - \left(\frac{\sigma}{r}\right)^{6}\right] \quad (1)$$

Here, r is the distance between atom centers, ε is the depth of the potential well, and σ is a characteristic atomic diameter (where $u_{LJ}(\sigma) = 0$). For larger components comprising many atoms, one may derive an analogous interparticle potential by summing the LJ interaction across all atom–atom pairs within the two particles. This procedure can be carried out analytically[68] for the case of two spherical particles of radii a_1 and a_2, and the resulting potential is – for small separations – approximated as

$$U_{LJ}(L) = \frac{2\pi a_1 a_2}{(a_1 + a_2)}\left[\frac{\pi\varepsilon(\sigma^6 - 210L^6)}{630L^7}\right] \quad \text{for} \quad L \ll \frac{a_1 a_2}{a_1 + a_2} \quad (2)$$

where $L = r - (a_1 + a_2)$ is the distance between particle surfaces. Figure 2a illustrates how this potential (for equally sized spheres) varies as the particle radius increases from atomic ($a = \sigma/2$, few Å) to nanoscopic dimensions ($a = 5\sigma$, few nm; $a = 50\sigma$, tens of nm). Regardless of particle size, the potential reaches its minimum value when the surfaces are separated by $\sim 0.6\sigma$; it follows that the length scale of the interaction is always of atomic dimensions. At the same time, the magnitude of the interaction increases linearly with particle size as $\sim 5\varepsilon a/\sigma$.

Remarkably, these scaling results are quite general – that is, they apply to other types of interaction potential – provided that the length scale of the interaction is much smaller than the dimensions of the particles. The famous Russian scientist Boris Derjaguin[69] was the first to show that in this limit, the interaction energy between two curved surfaces, U_{DA}, separated by a distance L can be derived from the corresponding potential (per unit area) for two flat plates, U_{FP}. For instance, for two spheres of radii a_1 and a_2, the Derjaguin approximation – one that we will encounter often in later sections – is given by

$$U_{DA}(L) \approx \frac{2\pi a_1 a_2}{(a_1 + a_2)}\int_L^\infty U_{FP}(z)dz \quad (3)$$

and similar formulas can be derived for interactions between two non-spherical bodies.[70] As in the LJ example, the magnitude of the interaction scales linearly with the size of the particles (for similar-sized particles), while the length scale of the interaction is independent of particle size. Consequently, the ratio of the interaction length scale and particle size decreases with the inverse of the latter, $\sim a^{-1}$. As we will see shortly (Section 2.3), this scaling can have profound effects on our ability (or inability!) to form self-assembled structures from increasingly large components.

2.2. Free Energy of Attraction

Given an interaction potential characterized by a length scale λ and magnitude ε, we now investigate whether or not this potential will cause the individual components (e.g., nanoparticles) to assemble spontaneously from solution. If these components are present in relatively dilute solutions, the attractive interactions mediating their assembly must be strong enough to overcome the entropic "penalty" associated with the loss of translational/rotation degrees of freedom upon aggregation.

To illustrate these effects, let us consider a model example of a system in which spherical particles interact via hard-sphere repulsions and attractive square-well potentials of depth ε and range λ. As the interaction magnitude ε increases, the particles begin to form small clusters before ultimately aggregating into a single bulk phase. The early stages of this process correspond to equilibrium cluster formation, for which the necessary statistical mechanical considerations are particularly simple. In this regime, the so-called equilibrium theory of physical clusters[71] can be used to relate the average numbers of n-sized clusters, N_n, to the canonical partition functions, Q_n, describing these clusters by the relationship $N_1^n/N_n = Q_1^n/Q_n$. In the simplest case of a two particle cluster, the number of dimers N_2 (concentration, c_2) may be expressed as

$$N_2 = N_1^2\left(\frac{V_\varepsilon}{8\pi V}\right)\exp\left(\frac{\varepsilon}{kT}\right) \quad \text{or equivalently} \quad c_2 = c_1^2\left(\frac{V_\varepsilon}{8\pi}\right)\exp\left(\frac{\varepsilon}{kT}\right) \quad (4)$$

where, $V_\varepsilon = \frac{4}{3}\pi[(2a + \lambda)^3 - (2a)^3]$ is the phase-space volume in which a particle interacts favorably with another particle. For small length scales, $\lambda \ll a$, this relation may be well approximated as $V_\varepsilon \approx 16\pi a^2\lambda$. With these considerations, the free energy (that is, a measure of both energetic and entropic effects) of dimer formation can be written as $\Delta F_2 = -kT\ln(Q_2/Q_1^2)$. Importantly, this free energy depends on both the magnitude of the potential (linearly, as $\Delta F_2 \sim \varepsilon$) and on its length scale (logarithmically, $\Delta F_2 \sim -\ln(\lambda)$ for $\lambda \ll a$).

To see how these scaling dependencies relate to the practice of self-assembly, assume we wish to assemble at least two-thirds of the free particles into dimers (so that $c_2 = c_1$). From Equation (4), this occurs when the magnitude of the interaction potential is $\varepsilon = -kT\ln(V_\varepsilon c_0/8\pi)$ or $\varepsilon \approx -kT\ln(2\lambda a^2 c_0)$ for small interaction length λ. For example, for a 1 μM solution of nanoparticles with radius $a = 20$ nm, the criterion for SA can be achieved using either short-ranged interactions ($\lambda = 5$ Å – e.g., vdW) of magnitude $\varepsilon \approx 8.3kT$ or longer range interactions ($\lambda = 50$ nm – e.g., electrostatic) with a magnitude of only $\varepsilon \approx 2.7kT$.

While the explicit expressions given above derive from simplistic interparticle potentials applied to "assemblies" of only two particles, the qualitative themes are general. First, the magnitude of the component interactions must be at least few times kT to induce assembly from solution (at high volume fractions, however, entropy alone can drive SA – even in the absence of attractive potentials; cf. Section 7.3). Second, more dilute solutions or shorter-range interactions require stronger potentials (i.e., larger ε) to overcome the unfavorable entropic effects accompanying the formation of a self-assembled structure. In this respect, strong, short-range interactions (large ε, small λ) may induce particle aggregation just as well as weaker, long-range interactions (small ε, large λ).

It must be remembered, however, that different potentials may result in different types of equilibrium assemblies. Furthermore, in addition to such thermodynamic considerations, the length scale of an attractive interaction (relative to the particle size) can have a profound influence on the kinetics of the assembly process, dictating the formation of either ordered structures or amorphous glasses/gels.

2.3. Order Versus Disorder: Further Implications for Nanoscale Self-Assembly

Most approaches to nanoscale self-assembly rely on the premise that carefully designed components and interactions should result in the formation of desired equilibrium structures corresponding to minima of the appropriate thermodynamic potentials such as Gibbs or Helmholtz free energies. In practice, achieving the equilibrium configuration is often a difficult task (e.g., in the case of protein crystallization[72,73]) but, even worse, it may prove physically impossible due to the competing formation of dynamically arrested glasses or gels.[74–76] Such non-equilibrium ''phases'' are characterized by long-lived, dynamically arrested states, in which the system's components become trapped in small regions of the overall phase space – where, in physical parlance, the system becomes non-ergodic.[77] Of particular interest in the context of self-assembly is the concept of ''attractive glasses'' (often termed ''gels'' at lower volume fractions), in which short-ranged attractive interactions induce the formation of ''frozen'' amorphous states rather than ordered equilibrium phases.[74,75] This competition between dynamical arrest and relaxation to equilibrium depends strongly on the length scale of the attractive interactions relative to the particle size, whereby particles interacting via short-range attractions are more susceptible to glass formation.[75]

These effects are illustrated in Figure 2b and c, which shows the theoretical phase diagrams for hard-sphere particles interacting via short-range attractive Yukawa potentials, $U_{YK}(r)$, with an attractive length scale, λ (scaled by particle diameter).[75]

$$U_{YK}(r) = \begin{cases} \infty, & r < 1 \\ -\varepsilon \dfrac{e^{-(r-1)/\lambda}}{r}, & r \geq 1 \end{cases} \quad (5)$$

In addition to the equilibrium phase boundaries, these diagrams show the dynamical arrest curves[74,76] to the right of and below which the system undergoes a transition from equilibrium/ergodic to trapped/non-ergodic behavior characterizing glass/gel formation. Even in the case of $\lambda = 0.2$ (typical of nanoscale particles; Figure 2b), we find that the solid crystalline regions of the phase diagram lie to the right of the dynamical arrest curve, indicating that glass formation will compete with crystallization (who wins this competition is a difficult question of kinetic control). As the length scale of the interaction decreases, the dynamical arrest curve shifts to even smaller volume fractions, enveloping more and more of the phase diagram (see Figure 2c corresponding to $\lambda = 0.03$). Thus, shorter-range interactions are increasingly likely to result in disordered glasses rather than order equilibrium structures.

In the context of self-assembly it is therefore desirable to use interactions that are of long range relative to the size of the assembling components. Unfortunately, many common attractive interactions (e.g., vdW forces) act appreciably over only molecular dimensions (cf. Section 2.1 and 6). In order to apply these molecular-scale forces in self-assembly, it is necessary to use small components – more precisely, nanoscopic components (e.g., ~2–30 nm) at most a few to tens of times larger than molecular length scales (3–10 Å). Larger particles such as micrometer-scale colloids interacting through similar short-range attractive potentials will invariably aggregate to form disordered precipitates or gels. Indeed, nearly all examples of colloidal crystallization rely on clever methods to overcome this potential limitation by using long-range interactions (electrostatic and depletion; cf. Sections 4 and 7.2, respectively) or by abandoning attractive forces in favor of entropic crystallization at high volume fractions (cf. Section 7.3). Of course, even at the nanoscale, self-assembly into ordered, equilibrium structures is by no means trivial, and the phase diagrams of Figure 2 offer further qualitative insights.

In addition to interaction length scale, the magnitude of attractive interactions mediating SA must also be chosen carefully. In Section 2.3, we discussed how strong such interactions must be to induce *any* form of aggregation (ordered or otherwise); however, there is also an upper bound on the interaction strength, above which SA gives way to precipitation, gelation, or glass formation (all forms of dynamical arrest). This is illustrated in Figure 2c, where an increase in the magnitude of the interaction ε, (or decrease in the temperature) at constant volume fraction first induces crystallization upon entering the fluid-crystal coexistence region but ultimately leads to formation of dynamically arrested states upon crossing the ergodic–non-ergodic transition curve. The ''optimal'' interaction magnitude for self-assembly is found between these transitions (region I) – this conclusion has been validated experimentally for protein crystallization[78] and is further discussed in Reference [75].

3. Van der Waals Forces

With these general considerations, let us first consider arguably the most ubiquitous form of nanoscale interaction. Van der Waals forces originate from the electromagnetic fluctuations due to the incessant movements of positive and negative charges within all types of atoms, molecules, and bulk materials. They are therefore present between any two material bodies, usually acting in an attractive fashion to bring the bodies together. The magnitude of these attractive interactions can be considerable – few to hundreds of times greater than kT – between even nanoscopic components. Because of this, vdW forces are often considered an untoward effect, causing the undesired precipitation of nanoparticles from solution. Through the use of stabilizing ligands or appropriate solvents, however, vdW interactions can be controlled to provide a useful tool with which to guide self-assembly processes – for example, that of 2- and 3D superstructures composed of nanoparticles[79,80] and/or nanorods[81,82] (Figure 3). Whether ones seeks to eliminate or to harness these ever-present forces, it is necessary to understand the various

small NANO MICRO

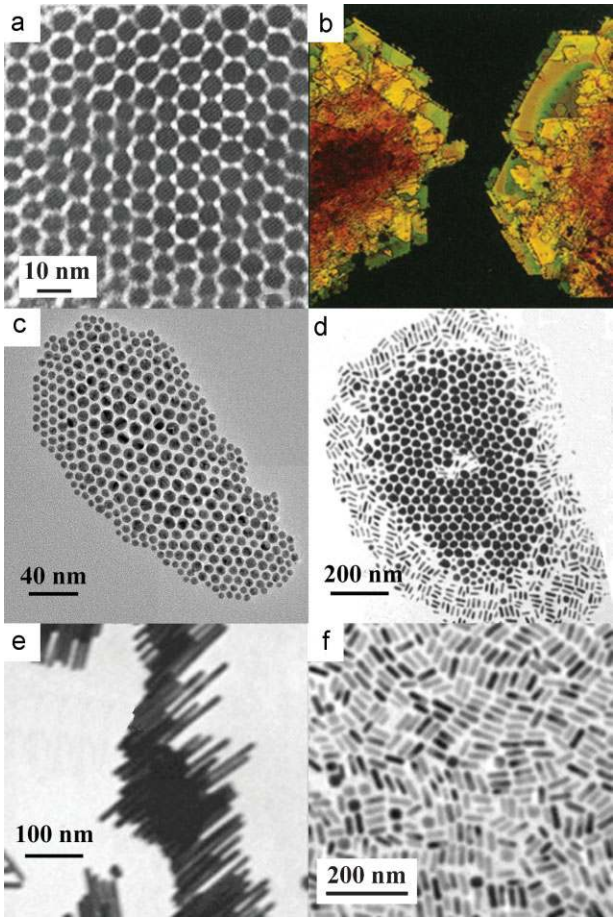

Figure 3. Different nanoparticle assemblies, the formation of which is driven primarily by vdW interactions. a) Two-dimensional hexagonally close packed structure of 5-nm Ag nanoparticles. Reprinted with permission from Reference [79]. Copyright 1996, American Chemical Society. b) Dark-field optical micrograph of faceted, three-dimensional crystals up to 50 μm in size, formed from 2-nm CdSe nanoparticles assembled into an fcc lattice. Reproduced with permission from Reference [80]. Copyright 1995, AAAS. c) Two-dimensional, size-segregated assembly of polydisperse gold nanoparticles stabilized by dodecylamine (DDA). The NPs adopt this configuration to minimize the total vdW energy of the aggregate (photo courtesy of R. Klajn). d) Another example of vdW-driven particle segregation based on both size and shape – here, separation of gold nanoparticles from smaller nanorods. Reprinted with permission from Reference [81]. Copyright 2005, American Chemical Society. e) Side-by-side organization of gold nanorods (15 nm by 200 nm) leading to continuous "ribbons" of particles. This behavior is observed for rods with aspect ratio larger than five. Reprinted with permission from Reference [81]. Copyright 2005, American Chemical Society. f) Isotropic assembly of gold nanorods the same as those in (e) but with an aspect ratio of 3.2. Reprinted with permission from Reference [81]. Copyright 2005, American Chemical Society.

theoretical approaches used to describe them and how to apply these methods towards the rational design of interparticle potentials mediating self-assembly at the nanoscale.

3.1. Hamaker Integral Approximation

The vdW interaction between atoms and/or molecules may be expressed by the well-known formula $u_{vdW}(r) = -C_{vdW}/r^6$ where r is the distance between atoms/molecules, and C_{vdW} is a constant characterizing the interacting species and the surrounding medium. Specifically, this constant derives from the sum of three distinct interactions, all of which scale with separation as r^{-6}: i) Thermally averaged dipole–dipole interactions (Keesom interaction),[65] ii) dipole-induced dipole interactions (Debye interaction),[65] and iii) the ever-present interactions between transient dipoles of polarizable bodies (London dispersion interactions).[83,84] The simplest approach to estimate the "macroscopic" vdW interactions between objects composed of many such atoms/molecules is a pairwise summation (or integration) of these molecular interactions throughout the volumes of the two bodies. This approach is identical to that described in Section 2.1 and results in the following approximate form for two spheres of radii a_1 and a_2 separated by a distance center-to-center distance r.

$$U_{vdW}(r) = \frac{A}{3}\left[\frac{a_1 a_2}{r^2-(a_1+a_2)^2} + \frac{a_1 a_2}{r^2-(a_1-a_2)^2} + \frac{1}{2}\ln\left(\frac{r^2-(a_1+a_2)^2}{r^2-(a_1-a_2)^2}\right)\right] \quad (6)$$

Here, A is the Hamaker coefficient, which, according to the Hamaker integral approximation,[85] corresponds to $A = C_{vdW}\pi^2/v_1 v_2$ where v_i is the molar volume of material i. For example, for hydrocarbons represented as a collection of CH_2 groups with $C_{vdW} \approx 50 \times 10^{-79}\,J\,m^{-6}$ and $v \approx 30\,Å^3$, the Hamaker coefficient is estimated to be $A \approx 5 \times 10^{-20}\,J$ (or $\sim 13\,kT$ at room temperature) across vacuum, which is very close to estimates derived from more rigorous treatments.[65]

While this approach provides a reasonable first-order approximation of both the magnitude and the distance dependence of vdW interactions across vacuum, it neglects i) many-body effects between atoms comprising the two bodies, ii) retardation effects due to the finite speed of light (important at large separations), and iii) discrete atom effects (important at small separations). The last assumption can be easily relaxed by performing a direct pairwise summation (instead of integration) between atom pairs; however, accounting for many-body effects and retardation require the use of more advanced theories of dispersion interactions. For these higher levels of approximation, we outline briefly two distinct approaches: the continuum Dzyaloshinskii–Lifshitz–Pitaevskii (DLP)[86,87] theory and the discrete coupled-dipole method (CDM).[88,89] The former provides an exact treatment of vdW interactions between continuum domains and incorporates many-body effects implicitly through the *bulk* dielectric response of the interacting materials and the surrounding medium. The CDM method follows a discrete approach akin to the Hamaker pairwise summation but accounting for all many-body effects. These effects become increasingly important at the nanoscale where the shape and size of a particle and the arrangement of its constituent atoms can dramatically influence the vdW interaction both at large separations[88] and near contact.[88,89]

3.2. Dzyaloshinskii–Lifshitz–Pitaevskii Theory

Although the theory of dispersion forces has been well established for almost 50 years,[86] the use of approximate forms (e.g., Hamaker integral approximation) persists largely due to

their simplicity relative to more rigorous treatments. The general treatment of vdW interactions in continuous media – originally due to Dzyaloshinskii, Lifshitz, and Pitaevskii (DLP)[86] – describes how correlations between the transient electromagnetic fluctuations within each material body give rise to attractive or repulsive interactions between them (repulsive vdW forces can arise between bodies of different materials interacting across a medium with dielectric properties intermediate to those of the two bodies; see References [90] and [91] for more detailed discussion of this intriguing phenomenon). As the frequency spectrum of these fluctuations is directly related (by the fluctuation–dissipation theorem) to the dielectric response of the bulk materials, these forces may be calculated directly from independent measurements of the electromagnetic adsorption spectrum for the materials involved. In this way, all many-body effects neglected by the Hamaker pairwise summation approach are completely accounted for within the empirical dielectric response of the relevant materials. The DLP theory thus enables direct calculation of the magnitude and distance dependence of the vdWs interaction between continuum bodies.

To illustrate how this approach compares with the simple Hamaker approximation, we first consider the model case of two coplanar semi-infinite media separated by a distance L. The Hamaker integral approximation estimates the interaction energy per unit area to be $U_{\mathrm{Ham}}(L) = -A/12\pi L^2$ with a constant Hamaker coefficient A. For comparison, the DLP result can be expressed in "Hamaker form", $U_{\mathrm{DLP}}(L) = -A(L)/12\pi L^2$, in which the Hamaker coefficient is no longer constant but depends explicitly on the separation L, as illustrated in Figure 4a. Specifically, $A(L)$ decreases rapidly with distance for $L > 10$ nm, and the vdW interactions become much weaker than would be predicted by the Hamaker integral approximation. These so-called retardation effects originate from the finite speed of light, which fails to maintain the correlations between electromagnetic fluctuations at large separations. In the context of nanoscale self-assembly, this means that vdWs forces become largely irrelevant when the surface separation exceeds ~10 nm. For smaller separations, the Hamaker coefficient may safely be treated as constant; however, the DLP theory remains invaluable for estimating its magnitude[92] (e.g., for gold across water, $A = A(L=0) \approx 9 \times 10^{-20}$ J [93]).

Although for non-planar bodies, the DLP-type approach becomes increasingly complex, it provides an accurate benchmark against which the approximations of Derjaguin[69] or Hamaker[85] may be tested. Figure 4b illustrates the performance of these approximations against the DLP solution[87,94] in the case of two equally sized (radius a) spherical gold particles in water. As the particles approach contact, both approximations approach the "exact" DLP result; however, significant deviations are observed at larger separations. For the Derjaguin approximation, $U_{\mathrm{Der}}(L) = -Aa/12L$, the separation between the surfaces, $L = r - 2a$, must be ~50 times smaller than the particle radius to obtain even modest accuracy of ~10%. Considering that the minimum possible separation is of molecular dimensions (e.g., ~1 nm for NPs covered with octanoic acid[95]), the Derjaguin method should be used with caution in the context of nanoscale self-assembly (e.g., for

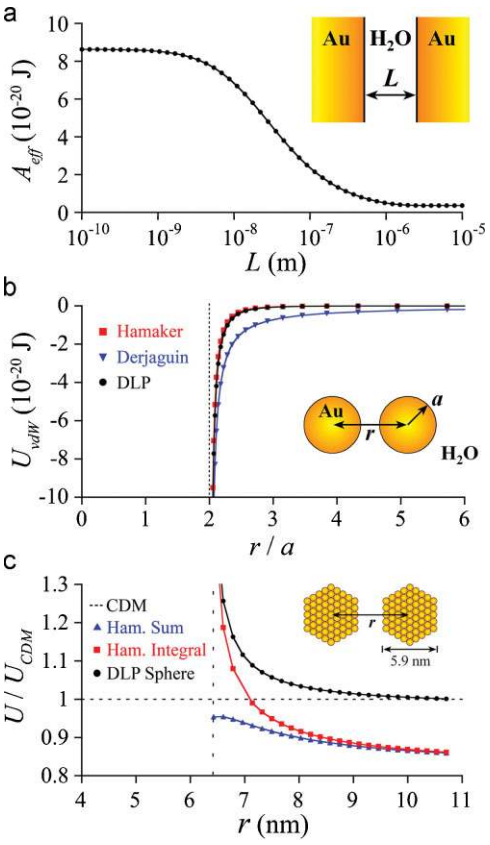

Figure 4. vdW potentials. a) Hamaker coefficient as a function of surface separation L, calculated using the DLP theory for two semi-infinite gold surfaces interacting across water.[93] b) Comparison of three continuum approaches to computing the vdW interaction between spherical gold particles interacting in water: the Hamaker integral approximation (red squares; Equation (6)), Derjaguin approximation (blue triangles), and the non-retarded DLP solution of Langbein[87,94] (black circles). c) Comparison of the continuum models of (b) with two discrete approaches: Hamaker pairwise summation (blue triangles) and the coupled-dipole method (horizontal dashed line). Adapted from Reference [89] for the case of dielectric nanoclusters.

$a = 5$ nm particles, the minimum separation is only ~5 times smaller than particle radius). The Hamaker approximation is more accurate, resulting in errors of less than 10% for surface separations below 0.1 a and below 30% for large separations (quoted errors are for the specific gold-across-water example; cf. Figure 4a,b).

Common to all continuum treatments of vdWs forces is the absence of a characteristic length scale (with the exception of retardation effects) and the divergence of the interaction energy at contact. Physically, the interaction energy at contact is finite due to repulsions between the finite-sized atoms comprising the interacting bodies, and the distance of closest approach is of atomic dimensions (cf. Section 2.1). When the surface separation approaches these atomic length scales, the continuum assumptions of smooth geometric surfaces and bulk dielectric properties come into question. Unfortunately, it is often the vdWs energy at "contact" that is most relevant to self-assembly, and the atomic/molecular structure[96] and dielectric properties[97] of nanoscopic components can deviate significantly from that of bulk materials – especially at the

small NANO MICRO

particle's surface. To account for these effects at small separations, we must return to a discrete description that accounts for all the many body effects neglected in the simple pairwise summation.

3.3. Coupled-Dipole Method

In this approach, the material body (e.g., a nanoparticle) is modeled as a discrete array of polarizable atoms represented by point electric dipoles at fixed locations (neglecting magnetic contributions and retardation). The dipole moment of each atom is related to the local electric field by the linear relation, $\mathbf{p}_i = \alpha_i \mathbf{E}(x_i)$, where $\alpha_i(i\omega)$ is the frequency-dependent polarizability of atom i. Here, the local field is due to all neighboring dipoles, each of which contributes $\mathbf{E}_j(x_i) = [3(\mathbf{p}_i \cdot \hat{\mathbf{r}}_{ij})\hat{\mathbf{r}}_{ij} - \mathbf{p}_i]/(4\pi\varepsilon_0 r_{ij}^3)$ to the total electric field at x_i. From the above relations, one can write a set of self-consistent equations for the N dipole moments and find the frequencies, ω, for which these equations are satisfied (i.e., the normal modes of the system). The free energy of the system is then readily calculated from these mode frequencies.[88,98,99] This approach has recently been applied to calculate vdW forces between nanoclusters of various shapes using the Drude model (i.e., treating atoms as classical, damped oscillators) for the atomic polarizability.

Figure 4c compares the results of the discrete CDM approach to those of the continuum DLP and Hamaker models for the case of two spherical particles 5.9 nm in diameter, each of which is composed of 1170 atoms positioned on a face-centered cubic (fcc) lattice.[89] Importantly, the two discrete approaches – the Hamaker pairwise summation and the CDM result – remain bounded as the particles approach contact and give realistic vdWs interactions at such small separations. In fact, the discrete Hamaker summation approach works surprisingly well (within 20%) at all separations. By contrast, the two continuum approaches – DLP sphere solution (Section 3.2) and Hamaker integral approximation (Section 3.1) – result in large errors at small separation due to their neglect of the discrete placement of atoms. At large distances, however, the more rigorous continuum treatment (DLP sphere solution) asymptotes to the correct value, while the Hamaker integral approximation does not.[100] Interestingly, the many-body corrections used in CDM and DLP methods become increasingly important for particles of anisotropic shapes. For example, many-body effects contribute as much as 50% to the overall interaction between highly anisotropic nanorods, for which the dielectric response of the particles themselves is anisotropic.[88] This situation is not uncommon at the nanoscale, where the size and shape of the particle can strongly influence the dielectric response of the material.[97] Thus, a practicing nanotechnologist working with small, anisotropic nanoparticles should consider using the CDM approach to accurately estimate the relevant vdW interactions. For more symmetric particles, however, higher-order corrections to the pairwise summation approach are typically small and can often be neglected in favor of the simpler pairwise summation.

In summary, continuum approaches cannot accurately predict the magnitude of vdW interactions at contact. Discrete CDM approach offers an attractive – albeit, computationally more demanding – alternative combining the advantages of the discrete Hamaker pairwise summation with a more rigorous treatment of many-body effects, characteristic of DLP-type calculations. In practice, many manifestations of nanoscale self-assembly (especially those in which particle surfaces are well-separated by stabilizing ligands) can be adequately described by simple analytical forms based on continuum theories such as the simplest Hamaker integral approximations or the DLP theories. However, for very small or highly anisotropic particles, in which the dielectric response deviates significantly from that of the bulk material, one should consider using the more accurate CDM-type approach to ensure that the model captures the physics of interacting nano-objects.

3.4. Illustrative Examples of Self-Assembly

The assembly of spherical, monodisperse NPs driven by vdW forces invariably results in the formation of close-packed structures such as hexagonal arrays in two dimensions[1,79,101,102] and close-packed crystals (hcp and fcc) in three dimensions[80,103] (Figure 3a,b). In many of these examples, ordering is achieved by gradually increasing the NP volume fraction (e.g., through solvent evaporation) until reaching a solubility threshold (determined by the magnitude of the attractions), upon which the NPs nucleate and grow to form ordered equilibrium structures. In such systems, however, it is often difficult to assess the role of vdW forces in the assembly process considering that similar behavior is also observed for non-interacting (or even, repulsively interacting) particles when the particle concentration exceeds a critical value (cf. Section 7.3 for more on entropy-driven self-assembly). Interestingly, close-packed structures are also obtained from polydisperse NPs,[104–106] in which vdW forces can order the resulting assemblies through a size-selective sorting effect. This effect is easily visualized in two dimensions (cf. Figure 3c) and results from the size-dependent magnitude of the vdW interaction (scaling as $U_{\mathrm{vdW}} \sim a$ at small separations and as $U_{\mathrm{vdW}} \sim a^6$ at large separations). Specifically, for finite-size, 2D superlattices, the overall potential energy of the system is minimized when the largest particles (strongest interactions) are in the center of the array and the smallest particles (weakest interactions) at the periphery.[104] NP segregation based on size-dependent interaction strength has also been used to separate nano-objects of different shapes (e.g., rods and spheres; cf. Figure 3d)[81] or to prepare increasingly monodisperse NPs by controlled precipitation of larger particles by addition of nonsolvent.[32,107,108]

Beyond the simplest case of spherical particles, vdW forces can result in highly directional interactions between anisotropic particles such as nanorods[81,82] and rectangular NPs.[81] For example, nanorods with large aspect ratios ($h/2a > 5$) assemble side by side to create large ''ribbons'', as illustrated in Figure 3e. The side-by-side configuration is strongly preferred due to the larger vdW forces as compared to those of alternative end-to-end assemblies. Applying the Hamaker integral approximation for small surface separations ($L \ll a$ and $L \ll h$), the vdW potentials for side-by-side and end-to-end configurations are given by

$$U_{\mathrm{SbS}} \approx -\frac{Aha^{1/2}}{24L^{3/2}} \quad \text{(cylinders, side by side)} \tag{7}$$

$$U_{EtE} \approx -\frac{Aa^2}{12L^2} \quad \text{(cylinders, end to end)} \tag{8}$$

When the ratio of these two interactions, $U_{SbS}/U_{EtE} \approx hL^{1/2}/2a^{3/2}$, is larger than unity, side-by-side assembly is preferred to end-to-end. For example, for gold nanorods ($a = 15$ nm and $h = 100$ nm) coated with cetyltrimethylammonium bromide (CTAB) ligands of length ~2 nm, the ratio at contact is $U_{SbS}/U_{EtE} \approx 2$, and "ribbons" are observed.[81] In contrast, for $U_{SbS}/U_{EtE} \approx 1$ (e.g., $a = 15$ nm and $h = 50$ nm), the assembly becomes more complicated with competing side-by-side and end-to-end arrangements observed in the same assembly (see Figure 3f).

4. Electrostatic Forces

Almost as ubiquitous as vdW forces, electrostatic forces provide a basis for the formation of ionic, colloidal,[109] and even macroparticle[110] crystals, and have recently been applied at the nanoscale[39,62,111] to form a variety of unique structures such as diamond-like NP crystals[39] and robust monolayer[112] or multilayer[113–115] surface coatings. Unlike vdW interactions, which are primarily attractive in nature, electrostatic interactions can be either attractive (between like-charged particles) or repulsive (between oppositely charged particles) and even directional, as in the case of particles with asymmetric surface-charge distributions[116] or permanent electric polarization.[117,118] Furthermore, the magnitude and length scale of these electrostatic interactions can be tuned controllably through the choice of solvent (e.g., dielectric constant) as well as the concentration and chemical nature (e.g., size and valence) of the surrounding counterions. Due to these unique attributes, electrostatic interactions are useful both for stabilizing particles in solution and for guiding their self-assembly into binary superstructures.

4.1. Electrostatics in Electrolyte Solutions

Before addressing the question of electrostatic interactions between charged particles, it is necessary to understand how the presence of dissolved ions influences the electrostatic potential, φ, within the fluid surrounding these particles. This problem is commonly addressed using the mean field Poisson–Boltzmann theory, which assumes pointlike ions (no volume) and neglects ion correlation effects.[119,120] Briefly, the chemical potential of positive and negatively charged ions is given by $\mu_\pm = \mu_\pm^o \pm e\varphi + kT \ln c_\pm$, where e is the elementary charge, and $c_\pm$ is the local ion concentration. At equilibrium, the chemical potential of ions is everywhere constant and equal to that of ions far from any charged surface, $\mu_\pm = \mu_\pm^\infty \equiv \mu_\pm^o + kT \ln c_s$, where the electrostatic potential is zero, and c_s is the bulk salt concentration. The local concentration of ions may then be written as $c_\pm = c_s \exp(\mp e\varphi/kT)$, and the local charge density as $\rho = e(c_+ - c_-)$ or $\rho = -2ec_s \sinh(e\varphi/kT)$. Substitution of this equation into Poisson's equation, $\nabla^2\varphi = -\rho/\varepsilon_0\varepsilon$, yields the nonlinear Poisson–Boltzmann[65,121] equation (originally due to Gouy,[122] Chapman,[123] and Debye and Huckel[124]) for a monovalent electrolyte.

$$\nabla^2\varphi = \frac{2ec_s}{\varepsilon_0\varepsilon}\sinh\left(\frac{e\varphi}{kT}\right) \tag{9}$$

Introduction of the dimensionless electrostatic potential, $\psi = e\varphi/kT$ (where $kT/e \approx 25$ mV at room temperature), gives the following representation characterized by a single parameter κ^2.

$$\nabla^2\psi = \left(\frac{2e^2c_s}{\varepsilon_0\varepsilon kT}\right)\sinh\psi = \kappa^2\sinh\psi \tag{10}$$

Here, $\kappa^{-1} = (2e^2c_s/\varepsilon_0\varepsilon kT)^{-1/2}$ is the so-called screening length, and it characterizes all parts of the system (i.e., near and far from charged surfaces) among which ions are equilibrated. Physically, κ^{-1} is the length scale characterizing the approximately exponential decay of the electrostatic potential upon moving away from charged bodies in solution. For example, in a 0.1 M aqueous electrolyte, the screening length is $\kappa^{-1} \approx 1$ nm.

4.2. Origins of Surface Charge

While Section 4.1 describes the equations governing the potential in electrolyte solutions, boundary conditions characterizing the surface of the charged objects are still needed to fully specify the electrostatics of the system. In general, surfaces become charged due to either the adsorption of charged (ionic) species onto a charge-neutral surface or the dissociation of ionizable surface groups (e.g., acidic groups under basic conditions). In either case, this adsorption/dissociation process is characterized by an equilibrium criterion (Figure 5a). In a simple case of acid dissociation $AH \leftrightarrow A^- + H^+$, this criterion is $\Gamma_{A^-}c_{H^+}/\Gamma_{AH} = K_d$, where Γ_{AH} and Γ_{A^-} are, respectively, the surface densities (i.e., number per unit area) of protonated and deprotonated surface groups, c_{H^+} is the H^+ concentration at the surface, and K_d is the equilibrium dissociation constant. Here, c_{H^+} is related to the concentration in the bulk solution, $c_{H^+}^o$, as $c_{H^+} = c_{H^+}^o \exp(-e\varphi/kT)$, such that $c_{H^+} > c_{H^+}^o$ near the negatively charged surface created by the deprotonated A^- groups. The surface charge density σ is directly related to the density of charged groups on the surface as $\sigma = -e\Gamma_{A^-}$ and is therefore related to the electrostatic potential at the surface as

$$\sigma = \frac{-e\Gamma_0}{1 + (c_{H^+}/K_d)\exp(-e\varphi_S/kT)} \tag{11}$$

where $\Gamma_0 = \Gamma_{A^-} + \Gamma_{AH}$ is the total density of surface groups. The derivation of a positively charged particle or charging via ion adsorption may be derived in similar fashion. Additionally, the charge density is related (through Gauss's law) to the electric field at the particle's surface, S, as

$$\sigma = \varepsilon_0(\varepsilon_P\nabla\varphi_P - \varepsilon\nabla\varphi)_S \cdot \vec{n} \tag{12}$$

NANO MICRO small

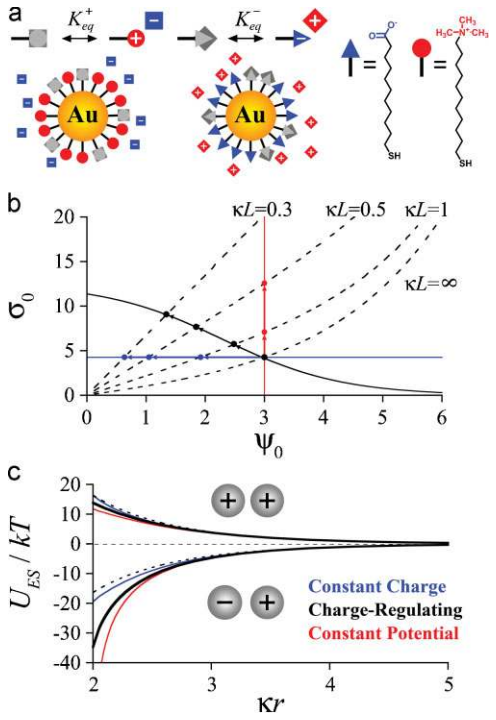

Figure 5. a) "Nanoions" composed of gold nanoparticles functionalized with negative (blue) and positively (red) charged ligands (right). Each ligand can be charged/dissociated (blue or red) or neutral (gray) due to the adsorption of an oppositely charged counterion; the equilibrium between these two states is characterized by an equilibrium constant K_{eq}, which depends on the specific ion/ligand pair. b) Illustration of the various boundary conditions in the case of two oppositely charged plates with surface potential, ψ_0 (in units of kT/e), separated by a distance L. The nonlinear Poisson–Boltzmann equation prescribes the surface charge density, σ_0 (in units of $\kappa kT\varepsilon_0\varepsilon/e$), as a function of ψ_0 and L (dashed curves). Additionally, σ_0 and ψ_0 are related through the appropriate boundary conditions: constant charge (blue), constant potential (red), and charge-regulating (black). The intersection between the dashed curves and the solid curves corresponds to the surface potential and charge density at equilibrium. c) Electrostatic interaction potentials between spherical nanoions illustrated in (a). Both repulsive and attractive interactions are illustrated using four different models. The dashed curve is the asymptotic approximation of Equation (16). The solid curves are calculated using the nonlinear Poisson–Boltzmann equation for different boundary conditions characterizing the particles' surfaces: constant charge (blue), constant potential (red), and charge regulating (black). Note that at any separation the magnitudes of "+/+" and "+/−" interactions are not of equal magnitude (see Section 4.5 for the explanation).

where ε_P is the dielectric constant of the particle, φ_P is the potential within the particle, and $\vec{n}$ is the outward surface normal.

Equating Equations (11) and (12) for the charge density gives the appropriate boundary conditions needed to solve the Poisson–Boltzmann equation derived in the previous section. This boundary condition is sometimes termed "charge-regulating"[125,126] due to the competing effects of the dissociation equilibrium (Equation (11)) and the ionic equilibrium characterized by the PB equation with the electrostatic boundary condition (Equation (12)). For the dissociation equilibrium, charge density should decrease with increasing surface potential; however, the PB equation requires that the charge should increase with increasing surface potential (Figure 5b). At equilibrium, both relations must be satisfied, and the dissociation/adsorption of ions from or onto the surface acts to maintain the surface potential at its equilibrium value – hence, "charge-regulation".

In the limit of $K_d \to \infty$, when all surface groups are dissociated/ionized, the charge-regulating condition becomes the more familiar constant charge boundary condition (Equation (12)) for which surface charge density σ is constant. Alternatively, in the limit of $K_d \to 0$ and $\Gamma \to \infty$ but with finite $\Gamma K_d \to$ constant, the charge-regulating condition becomes increasingly similar to the constant potential boundary condition (however, the two never formally converge; see Figure 5b). It is interesting to note that despite its ubiquity in the literature, the condition of constant surface potential has no physical basis in the surface equilibria responsible for charging. Nevertheless, these limiting behaviors – both constant charge and constant potential – remain useful both as approximations under appropriate conditions or as bounds on the more general charge-regulating model.

4.3. Free Energy of Interaction

Given the model of a charged surface described by the PB equation and the charge-regulating boundary conditions, the free energy can be calculated directly from the thermodynamic work required to charge the system by a reversible process.[121,126] Starting from a reference state, in which all surface groups are fully associated (i.e., charge neutral), the free energy of double-layer formation (per unit area) f may be calculated by the hypothetical charging process, in which Γ_{eq} ions (per unit area) are transferred from the surface into solution.

$$f = \int_0^{\Gamma_{eq}} (\mu_b - \mu_s) d\Gamma \tag{13}$$

Here, μ_b and μ_s are the chemical potentials of ions in the bulk electrolyte and on the particle's surface, respectively. It is assumed that μ_s is of the form, $\mu_s = \mu_s^*(\Gamma) + ze\varphi_s$, where z is the valence of the desorbing ions (e.g., $z = 1$ for the acidic groups discussed in Section 4.2); therefore, $\mu_b - \mu_s^*(\Gamma_{eq}) = ze\varphi_s$ at equilibrium. For the surface equilibrium model described in Section 4.2, Equation (13) may be rewritten as[126]

$$f = -\int_0^{\varphi_{eq}} \sigma d\varphi_s + kT\Gamma_0 \ln(1 - \alpha_{eq}) \tag{14}$$

where, α_{eq} is the fraction of dissociated surface groups at equilibrium. This quantity may then be integrated over the entire surface, S, of the particle(s) to give the total free energy F associated with double layer formation.

$$F = \int_S f dS \tag{15}$$

Finally, the interaction potential, $U_{es}(r)$, of two (or more) particles is simply the difference between the free energy of the ''interacting'' particles at finite separation and the free energy of the isolated particles: $U_{es} = F_2(r) - 2F_1$.

For spherical particles (radii a_1 and a_2) separated by distance r larger than the screening length, κ^{-1}, the interaction potential, U_{es}, is well approximated by the familiar DLVO (after Derjaguin, Landau, Verwey, and Overbeek) potential for screened electrostatic interactions.[121]

$$U_{es} = \frac{Q_1^{\infty} Q_2^{\infty}}{4\pi\varepsilon_0\varepsilon(1+\kappa a_1)(1+\kappa a_2)} \frac{\exp[-\kappa(r-a_1-a_2)]}{r} \qquad (16)$$

where Q_i^{∞} is the effective ''renormalized'' charge[120,127] on particle i, which characterizes the far-field potential about the isolated particle,

$$\varphi(r) \approx \frac{Q^{\infty}}{4\pi\varepsilon_0\varepsilon(1+\kappa a)} \frac{\exp[-\kappa(r-a)]}{r} \quad \text{for} \quad r-a \gg \kappa^{-1} \qquad (17)$$

In the linear regime ($e\varphi/kT < 1$), this renormalized charge is linearly related to the surface charge density, $\sigma_i^{\infty} = Q_i^{\infty}/4\pi a_i^2$, and the surface potential, $\varphi_i^{\infty} = Q_i^{\infty}/4\pi\varepsilon_0\varepsilon a_i(1+\kappa a_i)$, of an isolated particle. For highly charged objects (i.e., beyond the linear regime), however, the renormalized charge, Q_i, increases slower than linearly with the surface charge, σ_i^{∞}, saturating at the value $Q_i^{\infty} = 4\pi\varepsilon_0\varepsilon a_i(1+\kappa a_i)(4kT/e)$, corresponding to an ''effective'' surface potential of $4kT/e \approx 100\,\text{mV}$.[120]

While the above analysis is useful for particles separated by a large distance, it fails to describe the interactions between strongly interacting charged objects separated by distances that are small relative to the screening length, $r - a_1 - a_2 \leq \kappa^{-1}$. Given that the screening length can be as large as ~100 nm (for 10 μM aqueous electrolytes), these ''small'' separations are often not very small at all – especially in the context of nanoscale self-assembly. In this case, it is necessary to resort either to numerical methods or to make additional simplifying assumptions in order to keep the problem analytically tractable. For example, when the screening length is much smaller than the particle size, $\kappa a \gg 1$, we can apply the Derjaguin approximation (Section 2.1) and use the various analytical solutions for flat plates.[121,128] Furthermore, in the case of two weakly charged spheres (linear regime, $e\varphi/kT < 1$), there exist analytical solutions describing the free energy of interaction for various linear boundary conditions (constant charge, constant potential, and linearized charge regulation).[125]

4.4. Limitations and Extensions of the DLVO Potential

While the approximate form given by Equation (16) is used widely, it is important to understand its limitations, which arise due to the neglect of nonlinear effects in the Poisson–Boltzmann Equation (10) and of the boundary conditions at the particles' surfaces, which strongly influence the electrostatic interaction energy at contact. To illustrate these effects, consider a prototypical charged nanoparticle – the so-called ''nanoion''[129] used in the self-assembly of binary nanoparticle crystals[39] – comprising a 6-nm gold core functionalized with a self-assembled monolayer (SAM) of an ionic ligand, such as positively charged *N*,*N*,*N*-trimethyl(11-mercaptoundecyl)ammonium chloride (TMA) or negatively charged mercaptoundecanoic acid (MUA, pKa in NP/SAM ca. 6–8) at high pH. Such particles have ~500 charge groups on their surface, consistent with the surface density of thiolate monolayers on gold ($\Gamma = 4.7\,\text{nm}^{-2}$ [130]). Figure 5c illustrates the electrostatic interaction potentials between like-charged and oppositely charged nanoions assuming charge-regulating boundary conditions with an equilibrium constant of $K_d = 10\,\text{mM}^{-1}$ and salt concentration 10 mM (such that $\kappa a = 1$). At large separations ($\kappa r \gg 1$), the interactions are well approximated by Equation (16) using an effective charge of $Q^{\infty} = 26e$, which is considerably smaller than the ''bare'' charge of 500 e due to both the charge-regulating boundary conditions and the use of the nonlinear PB equation (necessary because of the large surface potential, $\varphi_S = 70\,\text{mV} > kT/e$). For smaller separations, however, the approximate form deviates from the charge-regulating interaction by ~20% for the case of like-charged particles and as much as 50% for oppositely charged particles at contact. The failure of the DLVO potential (Equation (16)) at small separations – well known to its original creators[121] – may result in qualitative discrepancies between self-assembled structures observed experimentally and those predicted theoretically on the basis of overly simplified interaction potentials (as in the case of diamond-like nanoparticle crystals[39] discussed in Section 4.5).

Additionally, the DLVO potential, which relies on the linear superposition of the electrostatic potential due to isolated particles,[131] does not account for changes in the electrostatic potential or the charge density at the surface of a particle in the presence (i.e., interacting with) a neighboring particle. To account for these changes, it is necessary to solve the Poisson–Boltzmann equation explicitly in the two-particle geometry and account for the specific boundary conditions characterizing the particles' surfaces. As illustrated in Figure 5c, the specific boundary conditions employed – e.g., constant charge, constant potential, or charge-regulating – can have a profound impact on the magnitude of the electrostatic interactions, especially at small separations. Here, the limiting cases of constant charge and constant potential provide upper and lower bounds on the charge-regulating interaction. For like-charged particles, the energy at contact is $\sim 6.4 \times 10^{-20}\,\text{J}$ ($\sim 16\,kT$ at room temperature) for constant charge and $\sim 4.8 \times 10^{-20}\,\text{J}$ ($\sim 12\,kT$) for constant potential; these values provide reasonably accurate bounds on the charge regulating result (e.g., $5.6 \times 10^{-20}\,\text{J}$ or $14\,kT$ for $K_{eq} = 10\,\text{mM}$). In the case of oppositely charged particles, however, these limiting cases are less useful as the constant potential result diverges to negative infinity while the constant charge result predicts a finite interaction energy of $8 \times 10^{-20}\,\text{J}$ ($\sim 20\,kT$) at contact – in other words, all we can say is that the ''real'' interaction energy must be something greater than $20\,kT$! Thus, reasonable estimates of the interactions between oppositely charged particles require the use of more exact treatment of the particles' surface equilibria.

The above example also highlights another, somewhat counterintuitive consequence of charge regulation – that is, the asymmetry between attraction and repulsion of opposite and like-charged particles. This effect is due to the desorption of bound ions from the NPs' surfaces in the regions of reduced electrostatic

small NANO MICRO

potential (cf. Equation (11)). Specifically, when oppositely charged NPs approach one another, the magnitude of the potential in the region between them decreases causing counterions to desorb. This desorption, in turn, increases the local charge density and the electrostatic interaction energy. In contrast, the magnitude of the electrostatic potential between proximal, like-charged NPs is enhanced, causing further adsorption of counterions, decrease in the local charge density, and reduction of the electrostatic interaction energy (see Reference [129] for more details). The differences in the like-charged and oppositely charged interaction potentials are of central importance in rationalizing the ionic-like behaviors of oppositely charged nanoparticles, such as their precipitation from solution only at the point of overall electroneutrality,[41,129] $\sum Q_i^+ + \sum Q_i^- = 0$ (reminiscent of the precipitation of inorganic salts at the solubility product).

4.5. Consequences for Self-Assembly

The charge-regulating potentials also have consequences for the self-assembly of nanoparticle superstructures driven by attractive electrostatic interactions. While few examples of electrostatic crystallization have been reported in the literature,[62,109] most explore crystallization at relatively high volume fraction ($\phi = 0.1$–0.7 upon evaporation of solvent[62]) with weak electrostatic forces ($Q = \pm 1e$ for 3–13-nm particles[62]). Although, under such conditions, crystal structures have been observed that are distinct from the close-packed arrangements driven by entropic effects (cf. Section 7.3), it is difficult to single out and assess the role of electrostatics among other competing effects driving the crystallization process. By contrast, Kalsin et al. observed the assembly of highly charged nanoparticles from very dilute solutions ($\phi \approx 0.01$) into open-lattice, diamond-like crystals (packing fraction of 0.34; cf. Figure 6). The formation of such "open" structures can be rationalized by electrostatic arguments using the appropriate charge regulating boundary conditions.

Specifically, while the positively and the negatively charged particles are exactly charge balanced (as verified by titration experiments[41,132]), the affinities of the charged ligands for their respective counterions may differ significantly – i.e., $K_d^+ \neq K_d^-$. This is especially the case for charged nanoparticles surrounded by monovalent counterions of appreciably different sizes – for example, in the system described in Reference[39] (like-sized NPs decorated with deprotonated MUA, or TMA alkane thiols), the NMe_4^+ and OH^- counterions have hydrodynamic radii of 1.8 Å and 0.4 Å, respectively. These differences in size result in different free energies of desorption, ΔG_d, which are determined primarily by electrostatic interactions between the charged ligand and the adsorbing counterion, $\Delta G_d \approx e^2/4\pi\varepsilon_0\varepsilon D$, where D is the ionic diameter.[133] For NMe_4^+ and OH^-, the free energies of desorption are estimated to be $\Delta G_d \approx 1.0 \times 10^{-20}$ J and $\Delta G_d \approx 4.4 \times 10^{-20}$ J, respectively (with $\varepsilon \approx 65$ corresponding to the DMSO-water mixture). Therefore, the desorption equilibrium constants, $K_d \sim \exp(-\Delta G_d/kT)$, are expected to differ by as much as four orders of magnitude, and the NPs have different effective charges (despite having the same numbers of thiols on their surfaces!).

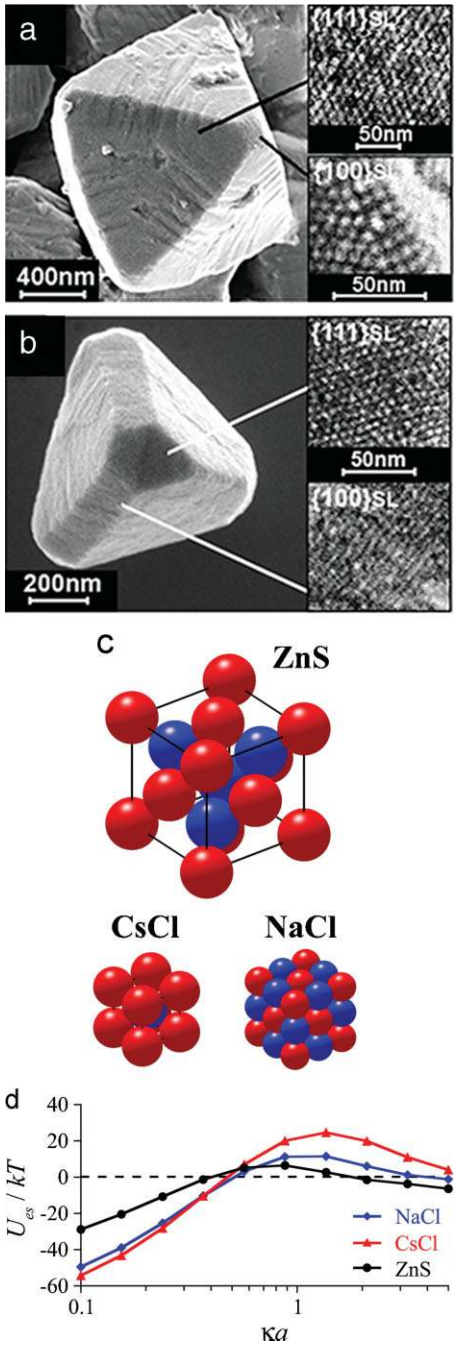

Figure 6. Electrostatic self-assembly of charge nanoparticles (cf. Figure 5a). a,b) Equally sized, oppositely charged nanoparticles – "nanoions" – assemble from solution to form the non-close-packed, diamond-like ZnS crystallites with octahedron (a) and truncated tetrahedron (b) morphologies. Reproduced with permission from Reference [39]. Copyright 2006, AAAS. c) Schematic illustration of the three 1:1 ionic lattices. The ZnS structure is found experimentally, despite its small packing fraction ($\phi = 0.340$) and low co-ordination number ($n = 4$) as compared to NaCl ($\phi = 0.524$, $n = 6$) and CsCl ($\phi = 0.680$, $n = 8$). d) Electrostatic free energy per particle for oppositely charged ($Q = \pm 500\,e$), 6-nm NPs organized onto one of the three 1:1 ionic lattices illustrated in (c). The equilibrium constants for ion desorption (scaled by the salt concentration) are $K_d^+/c_S = 100$ and $K_d^-/c_S = 0.01$, respectively. For small screening length ($\kappa a > 1$), the ZnS lattice is favored over NaCl and CsCl structures (note that the electrostatic free energy is actually positive under some conditions due to the strong asymmetry in the ionic equilibria).

This ''asymmetry'' in the surface equilibria can drive the formation of non-close-packed crystals, such as the diamond-like, ZnS structure. Indeed, for conditions similar to those used experimentally (cf. Figure 6d), the ZnS structure is more energetically favorable than the other 1:1 ionic lattices, NaCl and CsCl, which one would ''intuitively'' expect for like-sized, oppositely charged particles. In this context, it is interesting to note that formation of diamond-like crystals is possible only for small values of the screening length relative to the radius of the particles, $\kappa a > 1$. For larger screening lengths ($\kappa a < 1$), CsCl and NaCl are preferred due to their higher packing fractions – $\phi = 0.680$ and $\phi = 0.524$, respectively – resulting in the typical ordering of the electrostatic energies of ionic lattices, $U_{CsCl} < U_{NaCl} < U_{ZnS}$. At small screening lengths, however, only interactions between oppositely charged nearest neighbors and like-charged next nearest neighbors are important. In the ZnS lattice, the distance between next nearest neighbors is considerably larger than that in either CsCl or NaCl structures. Thus, upon decreasing the range of the electrostatic interactions, the decrease in the next nearest neighbor repulsions is most significant for the ZnS structure, while the attractive nearest neighbor interactions remain largely unaffected (cf. Reference [39] for more details).

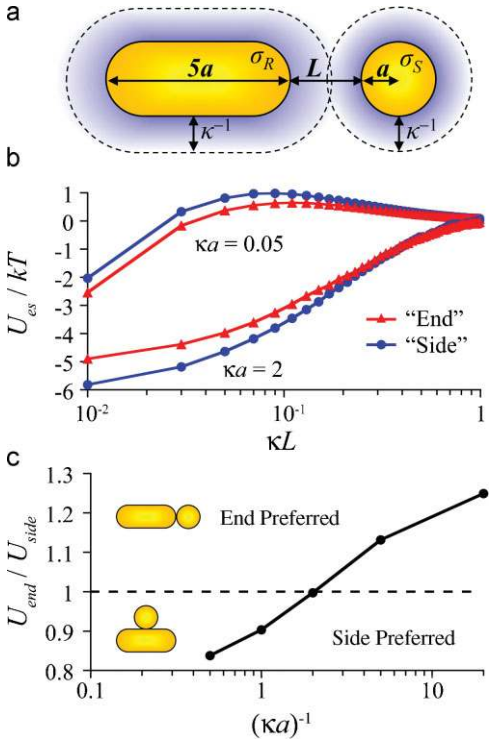

Figure 7. Electrostatic self-assembly of non-spherical particles. a) Schematic image of a charged AuNP interacting with an Au nanorod. The sphere and the rod have charge densities, σ_s and σ_r, respectively, with $\sigma_s = 20\ \sigma_r$. Owing to the large (infinite for ideal conductors) static polarizability of the gold particles, the dominant interaction is a charge-induced dipole interaction. b) Interaction potential as a function of distance for the ''side'' configuration and the ''end'' configuration for two different screening lengths. c) Ratio of the interaction energies at contact for the two configurations shown as a function of the screening length, κ^{-1}. Depending on the range of the electrostatic interactions, one of the two possible arrangements is preferred.

The formalism for treating electrostatic interactions developed in the preceding sections can be extended to non-spherical particles. Nanorods provide one interesting example whereby the preferred orientation of interacting particles may depend on the screening length (e.g., on the electrolyte concentration; Figure 7). Consider first the limit in which the screening length is much smaller than the dimensions of the particles, such that the Derjaguin approximation (Section 2.1) is valid, and the interaction depends only on the curvature of the interacting bodies near the point of contact. For example, a charged nanoparticle interacting with a longer, oppositely charged nanorod prefers to attach onto the ''side'' of the rod than at either of its two ends. In this case, the Derjaguin approximation predicts that the electrostatic interaction between a sphere (radius a_s) and a cylindrical rod (radius a_r, length h) with spherical ends scales as $U_{Side} \sim a_s a_r{}^{1/2}/(a_s + a_r)^{1/2}$ for the ''side'' arrangement and as $U_{End} \sim a_s a_r/(a_s + a_r)$ for the ''end'' arrangement, such that the former is always preferred. For larger screening lengths, however, for which the Derjaguin approximation no longer holds, the ''end'' arrangement may actually be the preferred configuration. As an example, consider a charged sphere interacting with a weakly charged but highly polarizable rod (e.g., a gold nanorod). Polarization of the rod by the sphere results in charge–dipole attraction, which at small separations can actually become stronger than the charge–charge interaction (c.f. Figure 7b). Due to the asymmetric shape of the rod, these polarization effects are most significant along the rod's longitudinal axis.[134]

To quantify these effects, consider the case of very large screening length, for which the sphere-rod interaction may be approximated as the sum of charge–charge and charge-induced dipole contributions neglecting ionic screening.

$$U(r) = \frac{Q_S Q_R}{4\pi\varepsilon_0\varepsilon r} - \frac{Q_S^2 V_R \alpha}{8\pi\varepsilon_0\varepsilon r^4} \tag{18}$$

Here, Q_S and Q_R are the charges on the sphere and on the rod, respectively, V_R is the volume of the rod, r is the center-to-center distance, and α is the rod's dimensionless polarizability, which depends on the orientation of the rod ($\alpha = 18$ when the rod is parallel to the line of centers and $\alpha = 2.1$ when it is perpendicular to the line of centers.[134]). When the sphere is at the ''side'' of rod ($r = 2a$; see Figure 7b), the magnitude of the charge–charge interaction is stronger than for the sphere at the rod's ''tip'' ($r = 3.5\ a$ for the system in Figure 7b). For charge-induced dipole interaction, however, the preference is reversed and this term might favor the ''tip'' configuration. This mechanism may be the cause behind the selective electrostatic adsorption of 5 nm Au nanoparticles onto the ends of larger Au nanorods observed experimentally.[135]

4.6. Beyond the Poisson–Boltzmann Equation

Despite the proven usefulness of the Poisson–Boltzmann theory of electrostatic interactions, some interesting effects are not captured by the above description. For example, the charge of a colloidal particle can actually change sign (so-called ''charge inversion''[136] or ''overcharging''[120]) in the presence

small NANO MICRO

of multivalent counter ions (see Reference [136] and references therein for experimental examples), and like-charged surfaces can attract one another at small separations due to electrostatic interactions mediated by divalent counterions[137,138] (see also Reference [139] and references therein). Neither of these phenomena can be explained within the mean-field approach described in Sections 4.1–4.3. The limitations of the Poisson–Boltzmann theory in these situations arise due to its neglect of correlations between the counterions, which become increasingly important for multivalent ions or low-dielectric (organic) solvents.[120] To account for these effects, it is necessary to resort to more advanced tools of statistical mechanics, such as integral equations[140,141] (often using hypernetted chain-like closures[141–143]), density functional theory,[144] or direct numerical simulation (often, Monte Carlo simulations[119,144,145] of the so-called primitive model, whereby ions are treated as charged hard spheres and the solvent as a dielectric continuum). As these approaches have been reviewed elsewhere in detail,[120,136,139,141] we highlight only briefly the interesting phenomena of charge inversion and like-charged attraction to illustrate the potential consequences of ion correlation effects at the nanoscale.

4.6.1. Charge Inversion

Consider an isolated, charged sphere with uniform surface charge density σ and radius a, such that the total charge on the particle is $Q = 4\pi a^2\sigma$ (valence $Z = Q/e$). In the presence of oppositely charged α–valent counterions, one might expect that N ions will adsorb (or ''condense'' [144,146]) onto the surface of the particle until the total particle–ion complex is charge neutral – that is, until $N_0 = Z/\alpha$. Under some circumstances, however, the number of condensed α-ions will be considerably larger than N_0, such that the net charge of the particle actually changes sign! To rationalize this counterintuitive result, let us consider the electrostatic energy of the particle-counterion system, U_N, in the zero-temperature limit (i.e., the minimal energy configuration).[120,147]

$$U_N = \frac{2\pi\sigma^2 a^3}{\varepsilon_0\varepsilon} - \frac{\alpha e a\sigma N}{\varepsilon_0\varepsilon} + U_N^{\alpha\alpha} \tag{19}$$

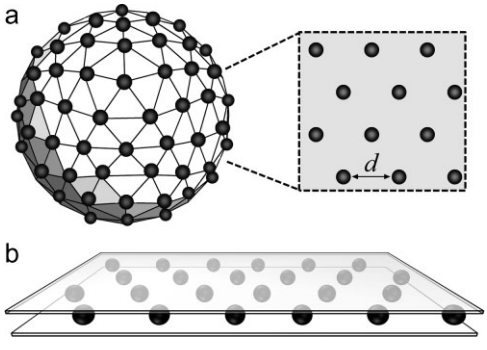

Figure 8. Ion correlation effects. Model geometries described in the text for the rationalization of a) charge inversion and b) like-charge attraction.

Here, the first term is the self-energy of the charged particle, the second term is the electrostatic energy of the condensedm α-ions in the field of the particle, and the third term is the repulsive energy between the like charged α-ions. The latter depends on the relative positions of the α-ions on the surface of the sphere. For example, if the positions of the α-ions are completely uncorrelated, they may be treated as a uniform shell of charge, such that $U_N^{\alpha\alpha} = \alpha^2 e^2 N^2/8\pi\varepsilon_0\varepsilon a$. With this assumption, the total energy, U_N, is minimal when $N = 4\pi a^2\sigma/e\alpha = N_0$. In other words, in the absence of counterion correlations, the energy is minimal when the total charge of the particle is neutralized by the oppositely charged α-ions.

In reality, the positions of the α-ions are correlated due to repulsive electrostatic interactions between them. Therefore, at zero temperature, the α-ions organize on the surface of the particle to form a triangular lattice (with few topological defects necessary to ''wrap'' around the sphere) in order to maximize the distance between their neighbors (Figure 8a). With this configuration, the unfavorable electrostatic energy between the α-ions can be calculated as[120]

$$U_N^{\alpha\alpha} = \frac{\alpha^2 e^2 N^2}{8\pi\varepsilon_0\varepsilon a}\left(1 - \frac{M}{\sqrt{N}}\right) \tag{20}$$

where $M = 1.106$ is the Madelung constant for the planar Wigner crystal (i.e., charges on a triangular lattice), which provides a good approximation as long as the characteristic distance between charges is much smaller than the radius of the sphere,[120,147] $(4\pi a^2/N)^{1/2} \ll a$. Substituting Equation (20) into Equation (19), the total electrostatic energy is minimal when

$$N = \frac{Z}{\alpha} + \frac{1 + \sqrt{1 + 4\gamma^2 Z}}{2\gamma^2\alpha} \quad \text{with} \quad \gamma = \frac{4}{3M\sqrt{\alpha}} \tag{21}$$

Thus, the effective charge of the particle, $Z_{\text{eff}} = Z - \alpha N$, is actually of opposite sign with respect to the bare charge.

$$Z_{\text{eff}} = -\frac{1 + \sqrt{1 + 4\gamma^2 Z}}{2\gamma^2} \tag{22}$$

Furthermore, Equation (22) predicts that the degree of ''overcharging'' increases with the bare charge of the particle (as $\sim\sqrt{Z}$) and with the valence of the counterions (as $\sim\sqrt{\alpha}$).

While the above considerations allow the rationalization of charge inversion in principle, its quantitative description for charge particles in electrolyte solutions at finite temperatures remains challenging.[120,136] More quantitative treatments of this phenomena have been proposed using a variety of theoretical and computation methods (see Reference [136] for more details).

4.6.2. Like-Charge Attraction

Another potential consequence of ion correlation effects is the short-range attraction between like-charged surfaces/particles – especially in the presence of multivalent counter

ions.[141] While the Poisson–Boltzmann equation invariably predicts repulsive interactions between like-charged particles,[148,149] attractive interactions in such systems have been demonstrated experimentally.[137–139,143] This phenomenon is most manifest in systems characterized by highly charged surfaces, multivalent counterions, and low-dielectric solvents, and occurs only when the two surfaces approach sufficiently close such that their ion condensation "shells" overlap.[141] Physically, this attraction arises due to correlations between ions condensed onto one surface with those on the neighboring surface. This can be illustrated for the case of two charged surfaces near contact, for which the condensed counterions are shared equally between the two surfaces. The number density (per unit area), Γ, of condensed α-valent counterions is determined by the charge-neutrality condition, $e\alpha\Gamma = 2\sigma$, where σ is the charge density on each of the surfaces. When the distance between α-ions, $d = (\pi\Gamma)^{-1/2}$, is significantly larger than the distance between the plates (cf. Figure 8b), this model system becomes directly analogous to the one component plasma in 2-dimensions, where the charge surfaces play the role of a uniform, neutralizing background charge.[120] As in the case of charge-inversion described in Section 4.6.1, we can estimate the electrostatic energy (per unit area) of this system in the zero-temperature limit

$$U = \frac{-Me^2\alpha^2}{4\pi\varepsilon_0\varepsilon d}\Gamma \qquad (23)$$

where $M = 1.106$ is the Madelung constant for the planar Wigner crystal. The electrostatic energy is favorable resulting in attractive interaction, whereby like charge surfaces are "glued" together via condensed counterions. In contrast, if the condensed ions were completely uncorrelated, the total electrostatic energy would be identically zero as the attraction between counterions and the surfaces is fully compensated by the repulsions between the two surfaces and between the counterions. In this case, the *free* energy of interaction would be repulsive due to the entropic penalty associated with ion condensation from solution. The distinction between these two scenarios (i.e., correlated vs. uncorrelated ions) is determined by the electrostatic coupling parameter, γ, where strong ion correlations arise only when

$$\gamma \equiv \frac{e^2\alpha^2}{4\pi\varepsilon_0\varepsilon d} \gg kT \quad \text{or equivalently} \quad \lambda_B\alpha^{3/2}(\sigma/e)^{1/2} \gg 1 \qquad (24)$$

Thus, strongly electrostatic coupling is achieved for large surface charges σ, ionic valence α, and/or Bjerrum lengths $\lambda_B \equiv e^2/4\pi\varepsilon_0\varepsilon kT$ ($\lambda_B \sim 0.7$ nm in water). In practice, multivalent ions are almost always needed to satisfy this condition even for the largest possible surface charge densities (typically, $\sigma \leq 0.5\,\mathrm{C\,m^{-2}}$). While the above description is overly simplistic (neglecting entropic effects, the finite sizes of the ions, image interactions due to dielectric boundaries, and the dependence on surface separation), the qualitative conclusions are general. More quantitative descriptions of the phenomenon of like-charge attraction have been derived using various theoretical methods[119,141,142,145,150] – typically, in the context of the primitive model (see Reference [141] and references therein).

4.6.3. Experimental Evidence and Challenges at the Nanoscale

Interestingly, while there exists considerable experimental evidence for like-charge attraction between planar surfaces,[137,138] rigid cylindrical macromolecules,[151] and flexible polyelectrolytes,[152] similar effects between spherical particles (most relevant to the present Review) remain somewhat controversial.[141] With some exceptions,[141,143] experimental studies focus on interactions between like-charge micrometer-sized colloids in *monovalent* electrolytes for which counterion correlations are negligible, and where the interaction potentials are found to be completely consistent with those derived from the Poisson–Boltzmann equation.[131,153] It is only for highly charged particles or macromolecules (e.g., DNA[151]) in the presence of multivalent counterions, for which deviations from the Poisson–Boltzmann theory may be expected. Exploring these effects in the context of charged nanoparticles should provide an important step towards validating existing theoretical predictions and elucidating the role of ion-correlations at the nanoscale.

In concluding our discussion of electrostatic interactions, we emphasize that the electrostatic charge on a nanoscale particle is predominately a surface effect – for example, through the adsorption or desorption of ionic species. Therefore, it does not preclude the presence of additional interparticle forces acting between the particles' volumes. In addition to vdW forces, other "body" forces arise between materials with a permanent electric or magnetic polarization. However, despite several interesting examples of electrically polarized particles (e.g., CdSe particles or other semiconductors),[118] these forces are typically weak and subject to screening in electrolyte solutions. More important in the context of self-assembly are interactions between magnetic components described in the next section.

5. Magnetic Interactions

Magnetic nanoparticles and their assemblies are sought in high-density storage of data[154] and magnetic energy,[155,156] magnetic separations,[157,158] drug delivery,[159,160] and hyperthermia treatments,[161,162] as well as in magnetic relaxation switches for sensing biological interactions between proteins, DNA,[163] and viruses.[164] When magnetic nanoparticles self-assemble, they tend to align their magnetic moments in the direction of the local magnetic field due to neighboring particles or applied fields. This gives rise to a specific directionality of interaction, enabling magnetic NPs to form micron-sized, one-dimensional chains/wires[165–168] or rings.[169,170] More recently, these NPs have also been shown to form two-dimensional aggregates[95,171,172] and even three-dimensional superlattices.[172–176] Controlling these self-assembly processes requires the understanding of the relationship between the magnetic properties and other particle characteristics such as size or shape. We first discuss some nanoscale-specific properties of isolated magnetic NPs.

NANO MICRO small

5.1. Isolated Magnetic Particles: Effects of Size and Shape

Magnetic particles come in many shapes and sizes ranging from nanoscale spheres[177,178] to micrometer-scale rods[179,180] and can be synthesized from a variety of magnetic materials including Co,[177,180] Fe_3O_4,[181] Fe_2O_3,[182] FePt,[183] Ni,[177] Mn_3O_4,[184] and MnO[184] (ordered by decreasing magnetic saturation). Magnetic nanoparticles are also synthesized by biological systems, for instance, by magnetotactic bacteria containing linear arrays of ~50-nm magnetite crystals[185] or in higher organisms where a protein called ferritin[186] is used for intracellular storage of iron and exhibits superparamagnetic properties characteristic of nanoscale magnets.

The properties of a magnetic material depend strongly on the particle size. Macroscopic ferromagnetic materials (e.g., Fe, Co, Ni) are composed of many micrometer-scale domains, in which the magnetic moments of the constituent atoms/molecules are aligned to yield a coherent magnetization below the so-called Curie temperature.[187] The net magnetization, however, may still be zero as the domain magnetizations are randomly oriented. For magnetic bodies smaller than the characteristic domain size (ranging from ~10 nm to 1 mm depending on the material[188,189]), this multidomain structure is no longer energetically favorable, and the material transitions to a single-domain ferromagnet. This single domain is characterized by a preferred or "easy" axis of magnetization that depends on both the crystal structure of the material and the shape of the particle. For example, in cylindrical Co nanoparticles of height h and radius a, the preferred magnetization is parallel to the axis of the particles for large aspect ratios ($h/2a > 1$) but orients along the radial direction for disk-like particles ($h/2a < 1$).[190] To the first approximation, the energy associated with deviations of the magnetization from the preferred direction is given by $E(\theta) = KV\sin^2(\theta)$, where K is the anisotropy constant, V is the volume of the particle, and θ is the angle between the easy axis and the magnetization. Thus, the "up" and "down" magnetizations ($\theta = 0$ and $\theta = \pi$) are equally favorable and separated by an energy barrier KV. The magnitude of this barrier depends on the size of the particle and distinguishes between two distinct magnetic regimes – that of ferromagnetism and superparamagnetism.

To illustrate this distinction, consider the time scale, τ, on which the particle magnetization flips spontaneously due to thermal fluctuations. This timescale is approximated[191] by the Arrhenius equation, $\tau = \tau_0 \exp(E_B/kT)$, where E_B is the energy barrier ($E_B = KV$ in the absence of applied fields), and τ_0 is a material-specific timescale (e.g., $\tau_0 \sim 10^{-9}$ s for 10 nm magnetite particles[192]). When the timescale for flipping, τ, is long compared to the relevant experimental timescales, the magnetic moment of the particle remains fixed (or "blocked") exhibiting ferromagnetic behavior with characteristic hysteresis in the magnetization curve upon changes in the applied field (it must be remembered, however, that even in this regime superparamagnetic behavior is possible if the particles are free to relax by a different mechanism – e.g., rotational diffusion of the entire particle, not just its moment, characterized by a time scale $\tau = 3V\eta/kT$, where η is the viscosity of the surrounding fluid). In contrast, when the experimental timescales are much larger than τ, the particle's magnetic moment fluctuates rapidly such that its time average, $\overline{m}$, is zero. Like paramagnetic atoms and molecules, such superparamagnetic particles exhibit a net magnetic moment only under an applied field, H, as characterized by the Langevin function, $\overline{m}/m = \coth(\eta) - 1/\eta$, where $\eta = mH/kT$, and m is the intrinsic magnetic moment of the particle. The approximate dividing line between ferromagnetic and superparamagnetic behavior is often set by the experimental timescale τ_{exp}, which can be used to define a "blocking temperature", $T_b = KV/k\ln(\tau_{exp}/\tau_0)$, above which a ferromagnetic material transitions to the superparamagnetic regime. For example, the blocking temperature of 26-nm iron oxide (Fe_3O_4 with $K \approx 1.1 \times 10^4$ J/m [193]) nanoparticles is ~300 K; therefore, at room temperature, particles larger than ~26 nm are ferromagnetic while smaller particles exhibit superparamagnetism.[92] Interestingly, close-packed arrays of magnetite NPs may exhibit ferromagnetic behavior even for particles smaller than 26 nm due to dipole–dipole interactions.[178]

In either regime, the magnitude of the intrinsic magnetic moment scales with the particle volume as $m = \mu_0 M_S V$, where μ_0 is the permeability of vacuum, and M_S is the saturation magnetization often equated with that of the bulk material, M_S^{bulk}. For magnetic particles in the nanometer size range, however, the magnetic saturation is typically smaller than the corresponding bulk value due to surface effects. Within the material, spins interact with one another to orient collectively in a single direction. Near the boundary, however, spins are increasingly disordered due to weaker coupling with the more ordered interior spins. This effect acts to decrease the saturation magnetization and may be approximated[194] as $M_S = M_S^{bulk}[(a-d)/a)]^3$, where a is the radius of the particle, and d is a characteristic thickness of the disordered surface layer (typically ~1 nm[195,196]). For example, for 9-nm $NiFe_2O_4$ particles, the saturation magnetization is estimated to be $\sim 1.6 \times 10^5$ A m^{-1}, which is significantly smaller than the bulk saturation of 2.9×10^5 A m^{-1} and agrees well with the experimental value of 1.8×10^5 A m^{-1}.[197]

5.2 Magnetic Interactions

The various size-dependent properties of single magnetic particles described above can have significant effects on the magnetic interactions driving self-assembly. The dominant contribution is the magnetic dipole–dipole interaction, derived here for spherical particles. A single magnetic sphere of radius a and constant, spatially homogeneous magnetization, $\mathbf{M}$, generates a magnetic field identical to that of a point dipole with magnetic moment, $\mathbf{m} = \mu_0 V\mathbf{M}$ with $V = \frac{4}{3}\pi a^3$.

$$\mathbf{H} = \frac{3(\mathbf{m}\cdot\hat{\mathbf{r}})\hat{\mathbf{r}} - \mathbf{m}}{4\pi\mu_0 r^3} \tag{25}$$

where $\hat{\mathbf{r}} = \mathbf{r}/r$ denotes the unit vector parallel to $\mathbf{r}$. The magnetic energy of such a dipolar particle in an external field, $\mathbf{H}$ (e.g., that due to a neighboring dipole), is given by $U_m = -\mathbf{m}\cdot\mathbf{H}$, such that the dipole experiences a force, $\mathbf{F} = \nabla(\mathbf{m}\cdot\mathbf{H})$. The dipole–dipole energy, U_{dd}, is simply the work required to bring two dipoles with moments, $\mathbf{m}_1$ and $\mathbf{m}_2$,

from infinity to a finite separation, **r**.

$$U_{dd} = \frac{\mathbf{m}_1 \cdot \mathbf{m}_2 - 3(\mathbf{m}_1 \cdot \hat{\mathbf{r}})(\mathbf{m}_2 \cdot \hat{\mathbf{r}})}{4\pi\mu_0 r^3} \tag{26}$$

Unlike the previous interactions discussed above, the dipole-dipole interaction is directional in nature and can be either attractive or repulsive (Figure 9a). For example, for "in line"

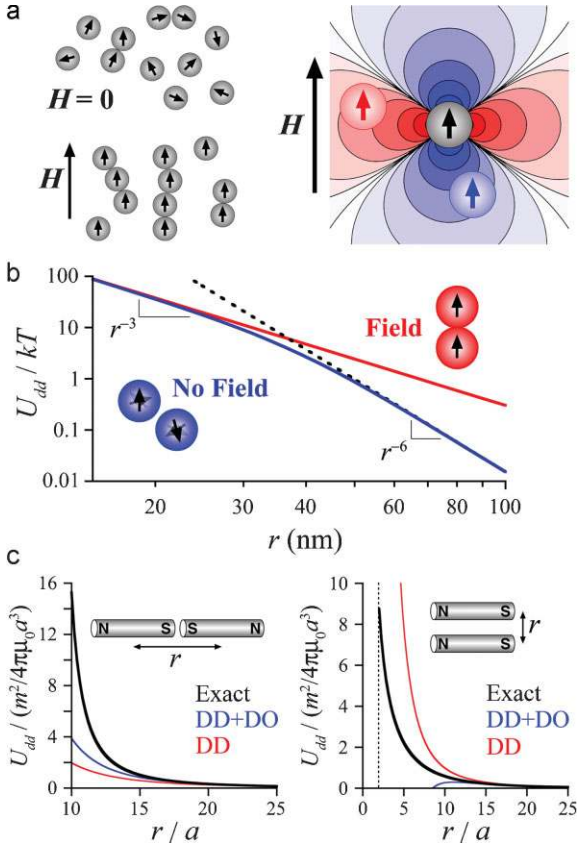

Figure 9. Interactions between magnetic nanoparticles. a) Schematic illustration of the behavior of weakly interacting magnetic particles. In the absence of an applied field, the particles' dipole moments (black arrows) are randomly oriented, and the particles remain largely unaggregated (top left). An applied field acts to orient the particles' moments in the direction of the field enabling the formation of chain-like aggregates (bottom left). The interaction between aligned dipoles can be attractive or repulsive, depending on the relative positions of the particles (right) – here, the blue regions denote attraction and the red regions repulsion. b) Interaction potential between superparamagnetic particles[198] – here 15-nm cobalt nanoparticles with magnetization $M_S^{bulk} = 1.4 \times 10^6\,A\,m^{-1}$. At small separations, the magnetic field due to one particle is strong enough to orient that of its neighbor, and the interaction is that of the most favorable "in-line" dipoles. At larger separations, however, the particles' moments become increasingly disoriented with respect to neighboring particles, and the potential approaches the Keesom interaction (dashed curve) decaying as r^{-6} as opposed to r^{-3} for "fixed" dipoles. This transition does not occur in a strong magnetic field, which maintains the relative orientations of the dipoles at any separation. c) Interactions between nanorods magnetized along their long axis and interacting end-to-end (left) or side-by-side (right). The three curves represent the exact potential (black; Equation (29)), the dipole–dipole approximation (red; Equation (26)), and the more accurate multipole approximation with the dipole-octapole correction (blue; Equation (28)).

dipoles (i.e., $\mathbf{m}_1 \cdot \mathbf{m}_2 = m^2$, $\mathbf{m}_1 \cdot \hat{\mathbf{r}} = \mathbf{m}_1 \cdot \hat{\mathbf{r}} = m$) the interaction is attractive with a magnitude $-m^2/2\pi\mu_0 r^3$; for dipoles aligned antiparallel (i.e., $\mathbf{m}_1 \cdot \mathbf{m}_2 = -m^2$, $\mathbf{m}_1 \cdot \hat{\mathbf{r}} = \mathbf{m}_2 \cdot \hat{\mathbf{r}} = 0$), it is repulsive with a magnitude $m^2/4\pi\mu_0 r^3$.

The magnitude of the interaction is characterized by the maximum magnetic energy at contact, $m^2/16\pi\mu_0 a^3$ or $\frac{1}{9}\pi\mu_0 a^3 M^2$, which can be considerable relative to the thermal energy, kT. For magnetite (Fe_3O_4) with a bulk magnetic saturation of $M_S^{bulk} = 4.8 \times 10^5\,A\,m^{-1}$, the characteristic dipole-dipole energy at room temperature for a 15-nm particle ($a = 7.5\,nm$) is $4.3 \times 10^{-20}\,J$ or $\sim 10kT$ at room temperature. Notice that this energy scales linearly with the volume of the particle, such that interactions between iron oxide particles smaller than ~7 nm, for which $U_{dd} < 1\,kT$, are too weak to induce self-assembly. For larger particles, however, magnetic dipole interactions can become *too* strong causing rapid flocculation in the absence of additional stabilizing forces (e.g., electrostatic or steric repulsions). Furthermore, these interactions are relatively long-range decaying as r^{-3} with no characteristic length scale. For superparamagnetic particles, however, the dipole–dipole interactions between fluctuating magnetic moments become weaker than those of "fixed" moments at large separations and are well approximated as

$$U_{dd}(r) = \frac{-1}{3kT}\left(\frac{m_1 m_2}{4\pi\mu_0 r^3}\right)^2 \quad \text{for} \quad \frac{m_1 m_2}{2\pi\mu_0 r^3} \ll 6kT \tag{27}$$

(Keesom Interaction)

Figure 9b shows distance dependence of the dipole interaction between superparamagnetic particles[198] and illustrates the transition from r^{-3} dependence for strongly correlated in-line dipoles to r^{-6} dependence for decoherent dipoles once the dipole energy falls below $\sim 6kT$.

For magnetic particles of more complex, anisotropic shapes the simple dipole–dipole expression becomes only a first approximation, which neglects interactions between the higher-order multipoles characterizing the fields surrounding each particle. For example, the magnetic field due to a cylindrical particle (height h, radius a) magnetized along its axis is characterized by a dipole moment, $m = \mu_0 M \pi h a^2$, an octopole moment, $Q_{30} = \frac{1}{4}\mu_0 M \pi h a^2 (h^2 - 3a^2)$, as well as other higher-order moments.[199] For two such cylinders, the second-order correction to the dipole–dipole interaction of Equation (26) is a dipole–octopole interaction, U_{do}, given by

$$\begin{aligned} U_{do} = \frac{mQ_{30}}{4\pi\mu_0 r^5}\Big[&\left[\tfrac{15}{2}(\mathbf{e}_1 \cdot \hat{\mathbf{r}}) + \tfrac{15}{2}(\mathbf{e}_2 \cdot \hat{\mathbf{r}}) - 3\right](\mathbf{e}_1 \cdot \mathbf{e}_2) \\ &-\left[\tfrac{35}{2}(\mathbf{e}_1 \cdot \hat{\mathbf{r}})^2 + \tfrac{35}{2}(\mathbf{e}_2 \cdot \hat{\mathbf{r}})^2 - 15\right](\mathbf{e}_1 \cdot \hat{\mathbf{r}})(\mathbf{e}_2 \cdot \hat{\mathbf{r}})\Big] \end{aligned} \tag{28}$$

where $\mathbf{e}_i = \mathbf{m}_i/m$ describes the orientation of cylinder i. The total interaction potential is then given by $U = U_{dd} + U_{do} + O(r^{-7})$. The effects of this second order correction are illustrated in Figure 9c for cylindrical particles of aspect ratio $h/2a = 10$ in both the "in-line" and "parallel" arrangements. For separations larger than $\sim \frac{3}{2}h$ (in general, the longest linear dimension of the particle), the first multipole correction provides an accurate approximation (within ~10%)

NANO MICRO small

to the exact interaction and is significantly better that the dipole–dipole approximation. Both approximations fail at small separations, at which increasingly many multipole moments are needed to make an accurate estimate.

In general, such higher-order corrections may be computed using methods developed for electrostatic problems and commonly used in physical chemistry to describe electrostatic interactions between molecules.[200,201] There, the multipole moments are calculated from the charge distribution of a given particle/molecule, and the interactions between such moments may be calculated using tabulated formulas.[200,201] In the case of magnetic particles, the ''magnetic charge'' distribution is analogous to the surface charge density of a polarized dielectric and is described by the quantity, $\sigma_m = \mathbf{M} \cdot \mathbf{n}$, where $\mathbf{M}$ is the magnetization, and $\mathbf{n}$ is the outward surface normal. While convenient and accurate for far-field interactions, the multipole approach becomes increasingly cumbersome for particles near contact due to the large number of terms needed in the expansion to obtain accurate results. Alternatively, one can calculate the magnetic interactions directly via numerical integration over the surface of the two particles as

$$U_m = \int_{S_1} \int_{S_2} \frac{\sigma_{m1}(\mathbf{r}_1)\sigma_{m2}(\mathbf{r}_2)}{4\pi\mu_0 r_{12}} dS_1 dS_2 \quad (29)$$

This procedure is used to obtain the ''exact'' interaction potentials between magnetic cylinders illustrated in Figure 9c. From these curves, we find that the end-to-end arrangement remains more favorable than the side-by-side configuration at all separations, in sharp contrast to the simple dipole-dipole form (Equation (26), which predicts the side-to-side configuration to be more favorable for rods at contact).

5.3 Illustrative Examples in Self-Assembly

Owing to the directionality of the dipole–dipole interactions, the types of self-assembled structures formed by spherical magnetic colloids are far richer than the simple hcp or fcc crystals whose formation is driven by all-attractive, spherically symmetric potentials (e.g., vdW forces; cf. Section 3). As the dipolar attraction is strongest between dipoles in the ''in-line'' configuration, magnetic particles assemble from dilute solutions to form linear chains[165–168] or rings[169,170] (Figure 10a,c) when the magnitude of the interaction exceeds $\sim 8kT$ (i.e., $m^2/16\pi\mu_0 a^3 \sim 8kT$).[202–204] For example, iron nanoparticles[205] coated with polyisobutene exhibit such ''string'' phases for 12-nm particles ($m^2/16\pi\mu_0 a^3 \sim 15kT$) but not for 10 nm particles ($m^2/16\pi\mu_0 a^3 \sim 5kT$). Upon further increase in the magnitude of the dipolar interactions (e.g., with increasing particle size), these linear chains begin to branch and ultimately percolate to form a connected, gel-like network.[202,206] For very strong dipolar interactions – typically induced by applied fields – magnetic NPs organize into superlattices characterized by body-centered tetragonal (bct) structures,[202] which have also been predicted by simulations of hard, dipolar spheres.[64] The above behaviors are observed at low to moderate NP concentrations; however, at higher volume fractions, organization of magnetic particles is driven more by entropic effects than by dipolar interactions resulting in fcc or hcp structures similar to those formed by ideal ''hard-sphere'' particles (cf. Section 7.3).

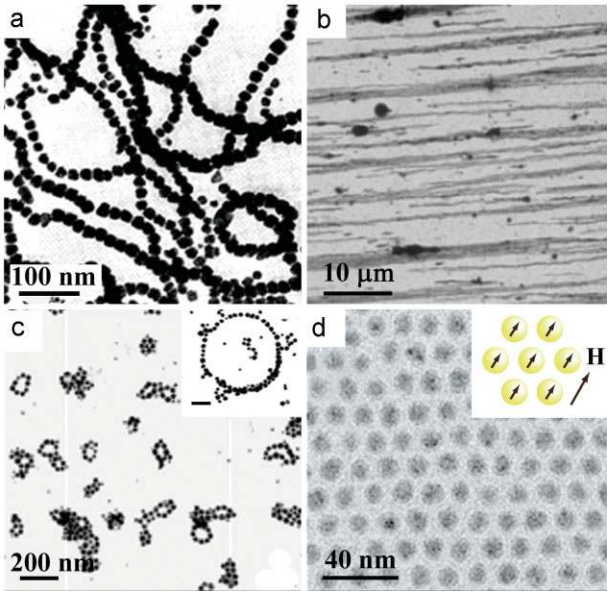

Figure 10. Self-assembly of magnetic nanoparticles by dipole–dipole interactions. a) Owing to their strong dipolar interactions, 20-nm cobalt nanoparticles form linear chains even in the absence of an external magnetic field. Reprinted with permission from Reference [165]. Copyright 1966, American Institute of Physics. b) TEM images of 10-nm γ-Fe_2O_3 nanoparticles, which organize into parallel chains (''nanowires'') under a magnetic field of 0.59 T applied parallel to the substrate. [95] The average length of the nanowires is on the order of 10 μm with a diameter of ~300 nm. Reprinted with permission from Reference [95]. Copyright 2004, Nature Publishing Group. c) TEM images of 27-nm cobalt nanoparticles forming rings[169] under a magnetic field of 0.225 T. Inset shows a ring with almost single-particle thickness. Scale bar is 100 nm. Reprinted with permission from Reference [169]. Copyright 2008, American Chemical Society. d) TEM images of 12-nm cobalt particles under a magnetic field of 1 T parallel to the substrate.[172] The particles form two-dimensional hcp arrays with an interparticle spacing of 12.2 nm. Reprinted with permission from Reference [172]. Copyright 2001, CSIRO Publishing.

When subject to a uniform magnetic field, H, the magnetic moments of the particles align with the applied field provided that $mH \gg kT$ (e.g., $H \geq 0.2$ T for 10-nm magnetite particles). In this case, interactions between oriented magnetic moments scale as r^{-3} at all separations (cf. Figure 9b), resulting in stronger dipole–dipole interactions as compared to those between superparamagnetic particles in the absence of the field. Thus, the applied field has two major effects on self-assembly: i) It induces the formation of aggregate phases from particles with smaller dipole moments than would be possible in the absence of the field (specifically, for $m^2/16\pi\mu_0 a^3 \sim 2kT$),[95,207] and ii) the phases that form are oriented with respect to the field (e.g., string phases shown in Figure 10b). In this way, using appropriately tuned magnetic particles, for which the characteristic dipole energy is between $\sim 2kT$ and $\sim 8kT$, it is even possible to induce assembly/disassembly on demand through the application/removal of an applied field[95,208] (a similar effect provides the basis for magnetorheological fluids[209]). Furthermore, because the

magnetic moments of all the particles are aligned coherently, magnetic self-assembly under an applied field can significantly improve the long-range order of the resulting structures.[172,174,210] For example, the domain size of two-dimensional superlattices of 12-nm CoNPs increases more than twofold (to 0.5 μm^2) in the presence of an applied magnetic field aligned parallel to the substrate. Aside from these distinctions, however, the structures formed under applied fields[172,203,207,210] are similar to those that form in the absence of fields.

In the derivations and examples so far, it was tacitly assumed that the magnetic dipole–dipole interactions were the sole forces responsible for particle assembly. In reality, magnetic interactions always compete with vdW forces (and possibly other types of forces) which become increasingly important with decreasing particle size. To see this, consider a pair of spherical particles coated with a SAM of thickness, δ, which prevents the particle surfaces from approaching closer than $\sim 2\delta$ (cf. Section 7.1 for a discussion of such steric repulsions). At contact, the magnitude of the vdW interaction is roughly $U_{vdW} \approx -Aa/24\delta$ (Derjaguin approximation, $\delta \ll a$), and the magnetic dipolar interaction is $U_{dd} \approx -\frac{1}{9}\pi\mu_0 a^3 M^2$. Thus, the vdW interaction scales linearly with the particle's radius, while the magnetic interaction scales with its volume. It follows that for sufficiently small particles and/or surface separations, δ, vdW interactions are expected to be the dominant contribution to the total interparticle potential. For example, in the absence of an external field, the experimentally observed[95] aggregation of 10-nm maghemite (γ-Fe_2O_3) nanoparticles can be attributed predominantly to vdW rather than magnetic forces. Only with the help of the strong external magnetic fields ($\sim$0.6 T), can the magnetic forces dominate self-assembly of such particles.[95]

6. Molecular Surface Forces

At the molecular scale, one finds a variety of short-range attractive forces – including covalent bonds, dipolar interactions, hydrogen bonding, donor–acceptor interactions, and so on – used to build complex molecules, crystals,[211,212] and supramolecular architectures.[213,214] Such interactions may also be employed at the nanoscale by decorating the surfaces of nanoscale components with various chemical functionalities. For instance, hydrogen bonds organize nanorods into linear chains,[215,216] divalent ''linkers'' such as DNA bring particles together selectively and reversibly,[217,218] and dipole–dipole interactions between photoisomerizable surface groups enable rapid assembly and disassembly of ordered nanoparticle structures.[219] In each of these examples, the specific molecular interactions give rise to significant and often specific interparticle potentials between much larger components and enable their spontaneous organization into a variety of order structures.

The magnitude of these surface forces is roughly equal to the number of individual bonds made (covalent or noncovalent) multiplied by an effective bond-strength characteristic of the molecular interaction. Thus, while the constituent interactions may be relatively weak (i.e., $\sim kT$), the forces between suitably functionalized surfaces can be quite strong due to the polyvalent interaction of several molecular groups. The length scale, λ, of these interactions is of molecular dimensions (angstroms to nanometers) and depends on the specific features of the interacting molecules (e.g., DNA mediated interactions are of longer range than hydrogen bonds between short chain ligands). At such short length scales, however, the distance dependence of the interaction is often of little importance, and the interactions may be treated as either ''on'' or ''off'' corresponding to particle surfaces separated by less or more than λ, respectively. Below we highlight four different molecular surface forces useful in nanoscale self-assembly: molecular dipole interactions, hydrogen bonding, DNA base-pair interactions, and reversible crosslinking interactions.

6.1. Molecular-Dipole Interactions

Molecules with a permanent electric dipole moment interact with one another via dipole–dipole interactions analogous to those between magnetic particles (cf. Equation (26)). The characteristic magnitude of these interactions is $\varepsilon_{dd} \approx p^2/2\pi\varepsilon_0\varepsilon\sigma^3$, where p is the dipole moment (typically, 0–4 debye), and σ is the minimal distance between dipoles. For example, for two *cis*-azobenzenes in contact with one another ($\sigma \approx 5$ Å, $p \approx 4$ debye), the dipole–dipole energy is $\varepsilon_{dd} \approx 2.7\,kT$ in toluene but only $\varepsilon_{dd} \approx 0.08\,kT$ in water due its large dielectric constant. In general, these molecular dipole interactions are only relevant in low-dielectric solvents; in water, charges (not dipoles) are needed to induce significant electrostatic interactions. Even in low-dielectric solvents, however, the dipole–dipole interactions are too weak to drive their alignment into the minimal energy, in-line configuration, and it is more appropriate to model them as thermally averaged interactions between freely rotating dipoles (Keesom interactions; cf. Figure 9b and Section 5.2), $u_{dd} \approx -(p^2/4\pi\varepsilon_0\varepsilon\sigma^3)^2/3kT$ at contact – e.g., $u_{dd} \approx 0.9\,kT$ for *cis*-azobenzene in toluene.

Although of relatively small magnitude, these molecular dipole interactions can become strong enough to induce self-assembly when several of them are tethered onto a particle's surface with density, Γ. In this case, the number of interacting dipole–dipole pairs between the two particles at contact may be approximated as $N_{dd} = \Gamma A_{eff}$, in which $A_{eff} \approx 2\pi a\sigma$ is the effective area of contact between spherical nanoparticles (NPs) of radius a. Thus, the total interaction energy due to molecular dipoles is approximately, $U_{dd} \approx u_{dd} N_{dd}$. For example, for $a = 3$ nm AuNPs functionalized with alkane thiols terminated with *cis*-azobenze, the surface density of these thiols is $\Gamma = 4.7\,nm^{-2}$ (i.e., one thiol per 21.4 $Å^2$ of Au surface[130]), and N_{dd} can be as large as $\sim$40 resulting in a total interaction energy of approximately 40 kT, which is $\sim$20 times larger than the vdW interaction for a surface separation of 1 nm. Clearly, when acting in concert, these molecular dipole interactions have the strength to induce self-assembly.

This particular example has already been realized experimentally using gold nanoparticles functionalized with mixed monolayers of azobenzene-terminated thiols and dodecylamine (DDA; Figure 11).[219] Interestingly, the conformation (*cis* or *trans*) of the azobenzene moieties may be controlled

NANO MICRO small

Figure 11. Self-assembly mediated by light-induced molecular dipole forces. a) Azobenzene thiol (AT) isomerizes from the *trans*- to the *cis*-conformation upon exposure to UV light. Importantly, the *cis*-isomer is characterized by a strong molecular dipole.[63,219] b) AT-functionalized nanoparticles self-assemble into various ordered structures in the presence of UV light due to molecular dipole interactions between the azobenzene groups tethered to their surfaces. Exposure to intense visible light induces the re-isomerization of the AT groups to the *trans*-conformation, and the loss of dipole–dipole interactions results in the dissolution of the NP structures.[63,219]

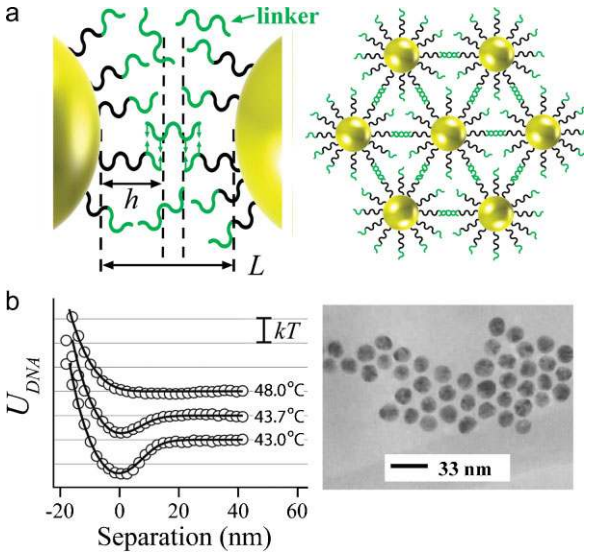

Figure 12. Nanoscale self-assembly via surface-grafted DNA. a) Schematic illustration of the DNA base-pair interactions between two nanoparticles (left) and one possible resulting self-assembled structure (right). b) The experimentally measured interparticle potential between DNA-functionalized AuNPs (circles) as well as the fit using the model described in the main text (note that interparticle separation is given relative to the minimum energy separation). The three curves (left) correspond to the three temperatures shown. Reprinted with permission from Reference [241]. Copyright 2005, American Physical Society. TEM image (right) of AuNPs self-assembled using the method shown in (a). Reprinted with permission from Reference [218]. Copyright 1996, Nature Publishing Group.

using light of different wavelengths: UV light induces *trans*-to-*cis* isomerization and visible light causes *cis*-to-*trans* re-isomerization. As only the *cis* isomer has an electric dipole moment, the molecular dipole interactions between the nanoparticles can be switched on and off by irradiation with light of different wavelengths. This approach has been shown to produce large, three-dimensional crystals (hcp structure) as well as disordered spherical aggregates.

6.2. Hydrogen-Bonding Interactions

As with dipolar interactions, hydrogen bonds are largely electrostatic in nature,[193,220] whereby a proton mediates the attraction of two larger atoms with partial negative charges. In addition to their widespread use in supramolecular systems,[213,214] these molecular interactions have also been applied to the self-assembly of larger nanoscale building blocks such as nanoparticles[221–224] and nanorods.[215,216,225] Magnitudes of individual hydrogen bonds range from 10 to 40 kJ mol^{-1} and depend strongly on the solvent conditions.[220] In general, the free energy of hydrogen-bond formation is significantly weaker in protic solvents (e.g., water, alcohols), in which molecule–solvent bonds are possible.

As in Section 6.1, the interaction energy between surfaces functionalized with hydrogen bonding groups may be approximated as $U_{hb} \approx u_{hb}N_{hb}$ at contact, where u_{hb} is the free energy of forming one hydrogen bond and N_{hb} is the number of such bonds made between the surfaces. This simple approximation neglects the effects of co-operativity between neighboring groups, however, these effects are often poorly characterized[226] and typically of little importance.[227,228]

At the nanoscale, hydrogen bonding has been shown to induce the aggregation of metal nanoparticles functionalized with hydrogen bonding ligands (e.g., HS–C_6H_4–X on gold with where X = OH, COOH, NH_2)[221] where the degree of aggregation and ordering depends on the strength of the individual hydrogen bonds formed. For example, very strong bonds between divalent hydrogen bonding molecules tethered to AuNPs induce rapid formation of fibrous NP gels[223] characteristic of strong, short ranged potentials. Hydrogen bonding can also be used in a more controlled fashion by site-selective functionalization of the particles[215,216] or by pH-responsive hydrogen bonding moieties.[221,225] The first approach has been used to create end-to-end assembles of gold nanorods mediated by hydrogen bonding functionalities tethered selectively to the ends of the rods.[215,216] When these groups are also acidic (e.g., carboxylic), the interactions are dependent on the pH of the surrounding solution, exhibiting strong hydrogen bond interactions at low pH and repulsive electrostatic interactions at high pH.[216] In this way, nanorods assemble end-to-end at low pH and disassemble at high pH; in between, however, the balance between hydrogen bond attraction and electrostatic repulsion gives way to side-to-side assemblies governed predominantly by vdW interactions. These relative simple examples illustrate the potential of using various interparticle interactions simultaneously to achieve a desired self-assembled nanostructure.

6.3. DNA Base-Pair Interactions

One very important type of hydrogen bond interaction is that between complementary DNA base pairs (adenine with

thymine; guanine with cytosine). These interactions are highly specific such that short DNA strands bind strongly only with complementary strands. Furthermore, by modulating the temperature below and above the melting temperature (typically, $T_m \sim 40\,^{\circ}C$ to $80\,^{\circ}C$ for oligomers of ~20 bases in a solution with 50 mM cations[229]), the interactions may be turned "on" and "off", respectively, enabling precise control over the magnitude of the attraction. These features make DNA-mediated interactions highly desirable for the self-assembly of nanoscale components.

This approach was first realized by the Mirkin group using gold nanoparticles covered with non-complementary DNA strands, which self-assemble upon the addition of a complementary DNA "linker" (Figure 12).[218] In similar pioneering work, Alivisatos et al.[217] exploited the directionality of DNA whereby Au NPs attached to either the 3′ or 5′ termini of complementary strands hybridize into head-to-tail or head-to-head dimers. Only a decade after these early demonstrations, DNA-based self-assembly has become the focus of entire symposiums[230] and has enabled the formation of complex assemblies such as nanoscale circuits from metals[59,231] and conductive polymers,[232,233] ordered arrays of nanorods[234] and proteins,[59,235] as well as nanoparticle chains,[235,236] rings, spirals, and, appropriately, double helices.[237] In the context of templated self-assembly, surfaces patterned with DNA (using an atomic force microscopy (AFM) tip) enable one to create arbitrary two-dimensional superstructures through the selective deposition of nanoscale objects bearing complementary DNA sequences.[238]

Many of these examples capitalize on the sensitive temperature dependence of DNA, which dissociates from its double-stranded helix into single strands over a narrow temperature range (typically ~30 degrees from completely dissociated to completely hybridized) centered about a "melting" temperature, T_m. This temperature is defined as one for which half of the DNA strands in solution are in the single-strand state and half are in the double-helix state.[239] In general, T_m depends on the strand concentration, the length of the strands, and even the specific nucleotide sequence (e.g., not only are G–C bonds stronger than A–T bonds but the bond energy is influenced also by the neighboring base pairs[239]). A widely accepted simplification in calculating bond energies and the melting temperature is the so-called nearest-neighbor (NN) model,[240] according to which the bond energy of any two base pairs is determined completely by the base-pairs immediately next to them. This results in only ten base-pair sets, for which the interaction strength – specifically, the enthalpy, ΔH_i^o, and entropy, ΔS_i^o, of forming a base-pair of type i – has been measured and tabulated extensively.[239] Furthermore, the NN model enables estimation of the melting temperature as $T_M = \Delta H^o/(\Delta S^o + R \ln C_T)$, where ΔH^o and ΔS^o are, respectively, the total enthalpy and entropy of DNA hybridization, and C_T is the molar concentration of DNA in solution (cf. Reference [239] for details).

For nanoparticles functionalized with complementary DNA chains grafted on their surfaces, the interaction energy at contact may be estimated crudely by simply summing the free energies of base-pair formation across all pairs as prescribed by the NN model (~1–2 kcal/mol per base pair). Such an approximation, however, neglects steric repulsions between the grafted chains, confinement-induced changes in the hybridization energy, and still leaves the problem of estimating how many DNA strands/base pairs actually bind together effectively. To remedy the situation, a more accurate interparticle potential has been developed to describe the interaction between colloidal spheres grafted with non-complementary DNA strands interacting in a solution of complementary DNA linkers (cf. Figure 12a).[241] The model includes an attractive force due to the dynamic forming and breaking of DNA "bridges" as well as steric repulsions due to compression of the DNA strands. Most importantly, the improved potential has been validated against experimental measurements.[241]

Assuming that the formation of each DNA bridge is statistically independent (i.e., neglecting intermolecular cooperativity between grafted DNA strands), the average attractive interaction is simply equal to the number of equilibrium DNA bridges formed, N_b, multiplied by kT.[241]

$$U_{DNA} \approx -kTN_b \tag{30}$$

At equilibrium, at a distance, x, from NP surface, the local concentration of bridges, $c_b(x)$, is related to the local concentrations of the linker, $c_l(x)$, and of the DNA's, $c_{DNA1}(x)$ and $c_{DNA2}(x)$, tethered to surfaces 1 and 2, respectively. The mass-action law[241,242] dictates that $c_b = Kc_l c_{DNA1} c_{DNA2}$ where $K = \exp(-\Delta G/kT)/c_0^2$ is the equilibrium constant for bridge formation, ΔG is the free energy of bridge formation, and $c_0 = 1$ M is a reference concentration (of the order of the solvent concentration). Here, the local concentrations of $c_{DNA1}(x)$ and $c_{DNA2}(x)$ are characterized by a probability distribution, $p_{DNA}(x)$, which depends on the specific model[243] used to describe the surface bound DNA (e.g., flexible chain, rigid rod, etc.). For two surfaces separated by a distance L (cf. Figure 12a), the concentrations, c_{DNA1} and c_{DNA2} are given by

$$c_{DNA1}(x) = c_{DNA2}(x) = \frac{\Gamma p_{DNA}(x)}{\int_0^L p_{DNA}(x)dx} \tag{31}$$

in which Γ is the surface density of DNA ligands, and the normalization factors ensure that the total number of DNA ligands per unit area is independent of surface separation. The total free energy per unit area of two interacting surfaces is then given by

$$\Delta f(L) = -\frac{kTN_b(L)}{S_A} = -\frac{kT\Gamma^2 c_l}{c_0^2}\exp\left(\frac{-\Delta G}{kT}\right)\int_0^L c_{DNA1}(x)c_{DNA2}(L-x)dx \tag{32}$$

where S_A is the area of the interacting surfaces. Assuming uniform distributions, $p_{DNA}(x) = 1/h$ for $x \le h$ where h is the "height" of the grafted DNA, and applying the Derjaguin approximation, Equation (32) leads to the following interac-

NANO MICRO small

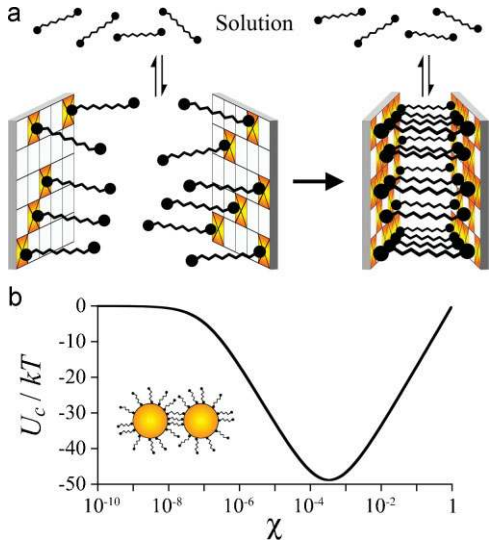

Figure 13. Crosslinking interaction. a) Divalent linker molecules free in solution adsorb onto individual surfaces (left) until equilibrium is achieved. Similarly, for two surfaces in close proximity, the linker molecules can bind to both surfaces (right), thereby crosslinking them together. b) The energy of this crosslinking interaction, U_c, for two spheres at contact depends on the mole fraction, χ, of linker molecules in solution. The plot here illustrates the interaction between 10-nm gold particles bound by short dithiol linkers ($\varepsilon = 8kT$, $\Gamma = 4.7\ \mathrm{nm}^{-2}$, and $\lambda = 0.1$ nm). Interestingly, the magnitude of the interaction is maximal at a particular concentration – approximately, $\chi \approx \exp(-\varepsilon/kT)$ for $\varepsilon/kT \gg 1$. Above this concentration, the coverage of dithiols linkers on the individual surfaces (a-left) approaches saturation, and the energetic difference between the individual surfaces (a-left) and the crosslinked surfaces (a-right) becomes increasingly negligible. Entropically, the crosslinked configuration remains preferred (the interaction is always attractive) as fewer linker molecules are required to adsorb from solution; however, the magnitude of this effect decreases with increasing linker concentration.

tion potential between spherical particles.

$$U_{\mathrm{DNA}}(L) \approx -\frac{kT\Gamma^2 c_l}{c_0^2}\exp\left(\frac{-\Delta G}{kT}\right)\frac{(2h-L)^2}{h^2} \quad \text{for} \quad h < L < 2h \tag{33}$$

The total interparticle potential for DNA-mediated interactions is illustrated in Figure 12b and combines the attractive interaction, U_{DNA}, with a repulsive steric potential described in detail in Section 7.1. This potential was found to be in quantitative agreement with experiment, even using the simplest nearest neighbor model for estimating the free energy of bridge formation, ΔG.

6.4. Crosslinking Interactions

In previous Sections, the molecular functionalities mediating attractive interactions were tethered permanently onto the surfaces of the assembling components. In addition, nanoparticles may also be assembled by the binding of divalent "linker" molecules dissolved in the surrounding medium – for example, gold NPs crosslinked by alkane dithiols[63,219] (Figure 13). Regardless of the specific nature of the linker molecule, the magnitude of crosslinking depends on the concentration of linkers in solution and on the energy of the bonds formed during crosslinking. These effects are captured by a simple equilibrium model of the crosslinking interaction between two planar surfaces described below.

When a single planar surface is immersed in a solution of divalent linkers, some will bind monovalently to the surface while others will remain in solution. The chemical potentials of the linker molecules in solution and on the surface are then approximated as, respectively,

$$\mu_s = \mu_s^o + kT\ln\chi \tag{34}$$

$$\mu_1 = \mu_1^o + kT\ln\left(\frac{\theta}{1-\theta}\right) \tag{35}$$

where μ^o is the standard chemical potential, χ is the mole fraction of linkers in solution, and θ is the fractional coverage of linkers adsorbed on the surface. These expressions assume ideal solutions and Langmuir-type adsorption equilibrium (no co-operative effects). At equilibrium, the chemical potentials for linker molecules on the surface and in solution are equal, $\mu_s = \mu_1$, such that

$$\frac{\theta_1^{eq}}{x(1-\theta_1^{eq})} = \exp\left(\frac{-\varepsilon}{kT}\right) \tag{36}$$

where $\varepsilon = \mu_1^o - \mu_s^o$ is the energy of adsorption – assumed equal to the strength of one bond between the linker molecule and the substrate (e.g., for thiols on gold, $\varepsilon \approx -3.2 \times 10^{-20}$ J [244]). The free energy per unit area, f_1, of this model system may be calculated by thermodynamic integration from the reference state ($\theta = 0$) to the equilibrium state ($\theta = \theta_{\mathrm{eq}}$).

$$f_1 = \Gamma\int_0^{\theta_1^{eq}} (\mu_s - \mu_1)d\theta = -\Gamma kT\ln(1-\theta_1^{eq}) \tag{37}$$

where Γ is the maximum surface density of linkers adsorbed onto the surface (e.g., $\Gamma \approx 4.7\ \mathrm{nm}^{-2}$ for thiols on gold[130]).

To derive the free energy of crosslinking of two surfaces, we assume that the bound linker molecules are attached to both surfaces, such that the chemical potential of bound linkers, μ_2, is given by equation (35) with $\mu_2^o \approx 2\mu_1^o$ (i.e., two bonds for each bound linker molecule). Thus, the free energy of formation (per unit area) for two cross-linked surfaces is given by $f_2 = -\Gamma kT\ln(1-\theta_2^{eq})$, and the free energy of crosslinking, Δf, may be expressed as

$$\Delta f = 2f_1 - f_2 = \Gamma kT\ln\left(\frac{1-\theta_2^{eq}}{(1-\theta_1^{eq})^2}\right) = \Gamma kT\ln\left(\frac{[1+\chi\exp(-\varepsilon/kT)]^2}{1+\chi\exp(-2\varepsilon/kT)}\right) \tag{38}$$

Here, the second equality is derived directly from Equation (36). In the limit of very dilute linkers, such that $\chi \ll \exp(2\varepsilon/\mathrm{kT})$, this expression simplifies to $\Delta f \approx -\Gamma kT\theta_2^{eq}$ – in other words, the free energy is proportional to the number

of crosslinker bridges formed at equilibrium. This was the approximation used in the DNA section (Equation (30)), however, in general the dependence is more complicated as illustrated in Figure 13.

Equation (38) may then be used to estimate the free energy of the crosslinking, U_c, between two spherical particles (radii a_1 and a_2) using the Derjaguin approximation discussed in Section 2.1.

$$U_c = \frac{2\pi a_1 a_2 \lambda}{(a_1 + a_2)} \Delta f \tag{39}$$

As before, λ is a characteristic length scale of molecular dimensions over which the crosslinking molecule can stretch (or compress) when bridging the two curved surfaces. Note that the explicit distance dependence has been neglected due to the short range of the interaction. In practice, such crosslinking interactions have been used to build three-dimensional NP crystals,[219] NP supraspheres ranging in size from 30–300 nm,[63,219] and even molecule-like clusters of asymmetric Au–Fe_3O_4 NPs.[245]

7. Entropic Effects in Self-Assembly

All the interactions we have described so far have their origins in the static or transient electromagnetic forces between atoms and molecules, working together to create various interparticle potentials between nanoscale components. Yet, even in the absence of attractive potential, self-assembly is still possible due to the so-called depletion forces or confinement effects. Common to these phenomena is the role of entropy, which can give rise to both attractive and repulsive interactions between components in dilute systems (Sections 7.1 and 7.2) or provide a driving force for order in concentrated systems (Sections 7.3). In this section, we survey how these purely entropic effects translate into effective interparticle potentials and how they can be harnessed for nanoscale self-assembly.

7.1. Steric Repulsion via Polymer Brushes

Given the potentially strong attractions between components due to, for example, vdW (Section 3) or surface forces (Section 6), these components may aggregate or precipitate uncontrollably thereby inhibiting the formation of ordered structures. Therefore, it is often desirable to complement the various attractive forces with "softer" repulsive interactions for which both the magnitude and length scale can be tuned appropriately to create effective interparticle potentials more amenable to controlled self-assembly. One approach is the use of electrostatic repulsions between like-charged components, which can be tuned by adjusting the ionic strength of the surrounding solution. Alternatively, particles may be stabilized by tethering long-chain molecules onto their surface to create repulsive steric forces upon compression of neighboring polymer "brushes".[246,247] This approach has long been used as a route to stabilizing colloidal particles;[66] however, it may also be used to engineer the potentials mediating nanoscale self-assembly (Figure 14).[95,248]

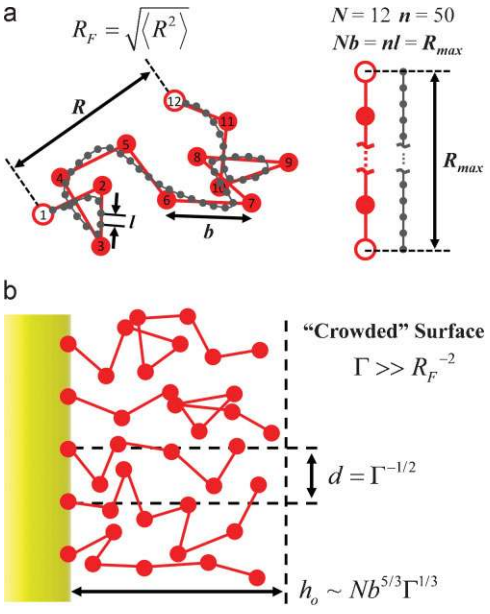

Figure 14. Visual glossary of polymer physics a) in solution and b) on surfaces. In solution, a polymer (*n* monomers; gray dots) with limited flexibility is idealized as a completely flexible freely jointed-chain, made of *N* segments of so-called Kuhn monomers, each of length *b*. Both the real and the idealized polymer have the same completely stretched length, R_{max}. The space that a polymer occupies in solution depends on its conformation; however, the root mean square of the end-to-end distance, *R*, is often used as a characteristic size – the so-called *Flory radius*, R_F. When grafted onto a surface, polymers will stretch out into solution to an equilibrium height h_0, that depends on the grafting density, Γ, and the number and length of the Kuhn monomers. When the distance between the grafted polymers, *d*, is much less than the Flory radius, then the polymers become "strongly stretched" such that brush thickness scales linearly with the number of monomers.

The theory of polymer brushes has been treated through various approaches including scaling theory,[249] self-consistent field (SCF) theory,[250–252] and Monte Carlo simulations[253] applied to both planar[249,251] and curved substrates.[250,252] Assuming that the polymer chains are well soluble in the surrounding solvent, a surface-tethered polymer brush is characterized by two length scales: the Flory radius of the polymer in its "random coil" configuration ($R_F \sim N^{3/5}b$ where *N* is the so-called degree of polymerization or, equivalently, the number of "Kuhn monomers" each with a characteristic length *b* [254]) and the average distance between grafting sites on the substrate, $\Gamma^{-1/2}$, where Γ is the surface density (Figure 15). Most relevant to nanoscale particles is the case of high grafting densities, $\Gamma \gg R_F^{-2}$, for which the polymers are stretched to an equilibrium length, h_0, which scales linearly[249,251] with the number of monomers as $h_0 \sim Nb^{5/3}\Gamma^{1/3}$ (e.g., $h \sim 5$ nm for 25-monomer polyethylene glycol grafted at a density of 1 chain per nm^2; $b = 1.1$ nm, $N \sim 4$ [254]). Specifically, in the so-called strong stretching[251] limit (for which the SCF treatment becomes analytically tractable), the equilibrium thickness, h_0, of the polymer brush as well as its free energy, *f*, (per unit area) may be approximated as

$$h_0 = N\left(\frac{12\Gamma b^5 \omega}{\pi^2}\right)^{1/3} \tag{40}$$

NANO MICRO small

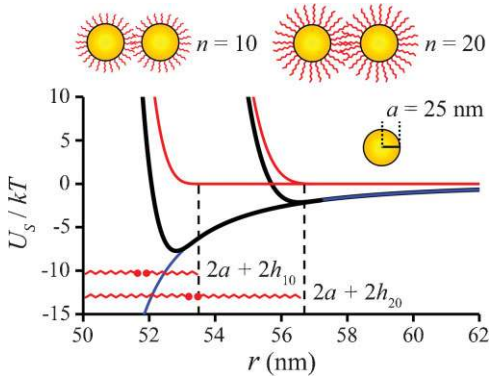

Figure 15. Engineering interparticle interactions with steric repulsion. The plot shows the total interparticle potential (black) between two 50 nm gold NPs derived as the sum of both van der Waals interactions (blue) and steric repulsions (red) due to polyethylene glycol ligands of two different lengths. The specific parameters used correspond to those described in the main text: $\Gamma = 1\ \mathrm{nm}^{-2}$, $b = 1.1$ nm, $\omega = 1$, and the number of Kuhn monomers, N, is related to the number of chemical monomers, n, as $N = 0.15\ n$ for $n = 10$ and 20, as illustrated in the figure.[254] Due to the compression of the ligands, the minimum energy separation is smaller than that of the extended ligands, $r - 2a < 2h$.

$$f(h) = \frac{\pi^2 kT\Gamma h_0^2}{6Nb^2}\left[\frac{1}{2}\left(\frac{h_0}{h}\right) + \frac{1}{2}\left(\frac{h}{h_0}\right)^2 - \frac{1}{10}\left(\frac{h}{h_0}\right)^5\right] \quad (41)$$

Here, ω is the excluded volume parameter, which characterizes the strength of the repulsive interactions between the chains ($\omega > 0$ in a "good" solvent). Inspection of Equation (41) reveals that the free energy increases monotonically upon compression ($h < h_0$) due to the increase in osmotic pressure within the brush. Qualitatively, this entropic repulsion derives from the osmotic pressure difference between the brush region and the solvent caused by the presence of flexible polymer chains, which behave like a semidilute "solution" of monomers within the brush. Thus compression requires work against the increasing osmotic pressure, and the resulting interaction is always repulsive. The magnitude of this interaction between two neighboring brushes can be estimated using equation (41) as $\Delta f(L) = 2[f(L/2) - f(h_0)]$, where $0 < L \leq 2h_0$ is the distance between the underlying substrates. While this model neglects polymer "interdigitation" as well as fluctuations about the polymer's minimum energy configurations, it has proven quite accurate in practice.[255]

For curved geometries, such as nanoparticles, Equation (41) may be used to derive the repulsive interparticle potential via the Derjaguin approximation (Section 2.1 and References [256,257]). Specifically, steric repulsion, U_S, between two spherical particles densely coated with long-chain ligands is given by

$$U_S(u) \approx \frac{2\pi a_1 a_2}{(a_1 + a_2)} \times \frac{\pi^2 kT\Gamma h_0^3}{6Nb^2}\left[-\ln u - \tfrac{9}{5}(1-u) + \tfrac{1}{3}(1-u^3) - \tfrac{1}{30}(1-u^6)\right] \quad (42)$$

where $u \equiv (r - a_1 - a_2)/2h_0$. While this equation provides a good approximation for short brushes, $h_0 \ll a$, it significantly overestimates the magnitude of steric repulsions for increasingly long brush lengths (cf. Reference [250] for a detailed comparison against full numerical solution for spheres).

Importantly, steric repulsion via long-chain ligands can be tuned to engineer interparticle potentials to yield desired structures. Consider the case of large, 50-nm gold nanoparticles functionalized with a polyethylene glycol brush grafted at a density $\Gamma = 1\ \mathrm{nm}^{-2}$ onto the surface. Here, the total interparticle potential consists of an attractive vdW interaction (Equation (6)) and the repulsive steric interaction (Equation (42)), which depends on the length and surface density of the stabilizing ligands. Figure 14 illustrates this potential for polymers of either 10 or 20 monomers, for which the equilibrium brush thicknesses are 1.8 nm and 3.6 nm, respectively. From the plot, we can see that the steric repulsion is actually quite "hard," such that the minimum energy separation between particle surfaces – 2.9 nm and 6.8 nm, respectively – is only slightly less than two times the equilibrium brush thickness. Hence, for the practicing nanoscientist using dense SAMs or polymer brushes, one may approximate the stabilizing ligands as hard shells and estimate the attractive vdW potential at a surface separation of $\sim 2h$. Corrections to this first-order approximation result in an increase in the magnitude of the vdW attraction at contact due to the compression of the SAMs – in other words, the true separation is smaller than $2h$. The magnitude of this effect increases with decreasing surface separation, for which the vdW attraction is stronger (e.g., the 2.9-nm brush is compressed more than the 3.6-nm brush).

For the total interaction potentials described above, the minimum energies are $-8\,kT$ and $-2\,kT$, respectively, for the short and long ligands (versus $-400\,kT$ for "bare" gold NPs without brushes). In this way, one can tune the interaction to the magnitude most appropriate for obtaining a desired self-assembled structure. This approach has been implemented in practice to control the relative strengths of vdW and magnetic dipole interactions mediating assembly of 10-nm maghemite (γ – Fe_2O_3) nanoparticles stabilized with ligands of varying lengths (e.g., 1.2-nm octanoic versus 1.6-nm dodecanoic acid).[95]

7.2. Attractive Depletion Forces

In addition to repulsive interactions, entropic effects can also lead to attractive forces between components as mediated by the presence of smaller particles or solvent molecules. This so-call depletion interaction was first explained by Asakura et al. using a model of hard-sphere particles immersed in a dilute "solute" comprising smaller hard spheres.[258] In this model, attraction occurs when the larger particles are so close together that no solute molecules can fit in between them, in which case the particles experience a net osmotic pressure acting to push them together. In the context of self-assembly, this depletion effect has been used to assemble linear end-to-end chains of cylindrical particles,[259] diblock-copolymer micelles,[260] and chains and/or dimers of platelet particles.[261] More generally, just as we were able to tune a purely entropic repulsive interaction in Section 7.1 by varying the length of the polymer/

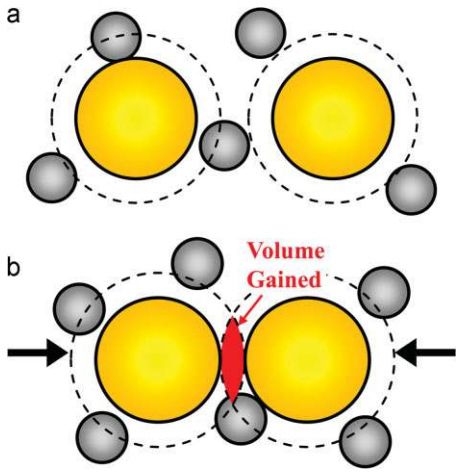

Figure 16. Depletion interaction. a) Illustration of gold nanoparticles immersed in a solution of smaller spherical macromolecules (gray spheres). The dashed lines illustrate the excluded volume regions into which the center of the solute particles cannot enter. b) As two particles approach, overlap of the excluded volume shells increases the volume available to the solute, decreasing the free energy of the system. Consequently, there is a mean force (black arrows) acting to push the particles together.

ligand layer, here we may tune a purely entropic attractive interaction by adding solutes of particular sizes and concentrations to our system. Below we outline Asakura's original model[262] and discuss how it can be used to engineer self-assembly processes at the nanoscale.

Consider two "hard" particles of radius a immersed in a dilute solution of smaller hard spheres (e.g., representing dissolved polymer species) with diameter σ, which is assumed to be significantly larger than that of the solvent molecules. With this assumption, the solvent may be treated as a uniform continuum in which the particles and the solute interact. Specifically, as the particle surfaces approach a separation smaller than the diameter of the solute, the total volume available to the solute increases due to overlap of the excluded volume "shells" surrounding each particle (Figure 16). The increase in available volume results in a decrease in the free energy of the overall system, defined as $F = -kT \ln Q$, where Q is the canonical partition function. For dilute solutions, the partition function is well approximated as $Q = V^N$, where N is the number of solute species, and $V = V_0 + \Delta V(r)$ is the volume accessible to the solute expressed in terms of the total volume, V_0, and the volume gained, $\Delta V(r)$, as the separation between the particles decreases. Thus, the free energy of the system is given by

$$F = -NkT \ln[V + \Delta V(r)] \approx -NkT\left[\ln V_0 + \frac{\Delta V(r)}{V_0}\right] \tag{43}$$

and the free energy of interaction by $\Delta F(r) = F(r) - F(\infty) = -NkT\Delta V(r)/V_0$. Notice that the interaction is directly proportional to the osmotic pressure, $p_0 = NkT/V_0$, of the solution, such that the magnitude may be tuned by varying the concentration of dissolved species. In the case of spherical particles and solute species, the distance dependence of the interaction potential becomes a simple geometric problem resulting in the interaction potential

$$U_{\text{dep}}(r) = -\frac{\pi p_0}{12}[2(2a+\sigma)^3 - 3(2a+\sigma)^2 r + r^3] \quad \text{for} \quad 2a < r < 2a + \sigma \tag{44}$$

The length scale of the depletion potential is clearly σ, and it reaches its maximum value of $U_{\text{dep}}(r) = -\frac{\pi}{6}p_0\sigma^2(3a+\sigma)$ when $r = 2a$. For spherical particles, the magnitude of this interaction increases with increasing size and concentration of the solute species, but is typically less than the thermal energy, kT. For example, the depletion interaction between polystyrene spheres, $a = 300$ nm, mediated by a smaller polystyrene "solute", $\sigma = 65$ nm, present in a volume fraction of 0.2 yields an interaction energy at contact of only $U_{\text{dep}} \sim -0.2\,kT$, insufficient to induce aggregation.[263]

This interaction is much stronger, however, when spherical particles are immersed in solutions of highly asymmetric solutes (e.g., rigid long-chain macromolecules), or when they interact with planar or concave surfaces. In the case of asymmetrical solutes, the interaction potential is determined through geometrical arguments similar to those derived above but accounting for the possible orientations of a solute in between the larger particles.[262,264] Specifically, for long ellipsoidal solutes (σ_A long and σ_B wide with volume v), the depletion potential for two spheres at contact is given by

$$U_{\text{dep}}(2a) = -\frac{p_0 a v}{\sigma_A}\left[\left(\frac{\sigma_A}{\sigma_B}\right)^2 + 2\right] \tag{45}$$

This expression assumes that $a \gg \sigma_A$ and, as expected, converges to the symmetrical case of equation (44) when $\sigma_A = \sigma_B$. For example, the energy of attraction between 50 nm spheres dispersed in a solution of macromolecular "ellipses", 20 nm long and 1 nm wide, is $\sim 5\,kT$ at even small solute volume fractions of 0.01. The range of this interaction is characterized by the longest dimension of the solute particle, and the theoretically predicted increase in the magnitude of the interactions is strongly supported by experiments using rigid, long-chain macromolecules.[262,264]

A fundamentally different, but equally effective variation on the sphere–sphere depletion potential is the interaction between spheres and planar or concave surfaces. Intuitively, it is clear that the interaction between a sphere and a concave surface will result in a much larger increase in solute free volume than that between a sphere and a convex surface. Indeed, spherical particles adsorb strongly into concave wells patterned on two-dimensional substrates in the presence of smaller polymer solutes. The depletion interactions mediating this form of templated self-assembly are an order of magnitude larger than those between the spherical particles themselves.[265] Interestingly, such particle–template interactions driven by entropy have recently been suggested as a driving force for the "lock-and-key" behavior of some enzymes[266] and provide a attractive approach towards templated self-assembly.

NANO MICRO small

7.3 Entropic Ordering at High Volume Fractions

In Section 7.2, we attributed the depletion interactions to the increase in free volume available to *solute* particles upon reconfiguration of *larger* particles. In this analysis, we considered only dilute solutions for which it was safe to assume that each solute species interacts independently of the others to give an additive contribution to the overall interaction. In concentrated systems, however, large particles may conspire (by chance, of course) to create hollow, multiparticle ''enclosures'' into which other particles cannot fit. Since such reduction in the available volume is entropically unfavorable, the system maximizes its entropy (thereby minimizing its free energy) by phase transitioning into an ordered phase, in which the particles maximize the ''free'' volume available to them.

In general, entropy-driven formation of ordered phases requires volume fractions, ϕ, that are high enough such that the average interparticle distance – $d \approx (2V_p/\phi)^{1/3}$ where V_p is the particle volume – is smaller than the largest linear dimension of the particles. Hard-sphere ''liquids'', for example, are well known to undergo a phase transition to form a crystalline fcc structure at a volume fraction of $\sim$0.494 as demonstrated through experiments and simulations dating back to 1957.[267–269] On the other hand, hard rods (e.g., often studied as a model system of Tobacco mosaic viruses, TMV[270]) form ordered phases at volume fractions in solution as low as $\phi \sim 0.05$, since the excluded volume between two rods is much larger than the volume of the rods themselves (Figure 17; for TMV, $d \approx h(\pi/2\phi R^2)^{1/3} \approx 0.3h$ where $R \equiv h/2a = 37$ is the aspect ratio). Interestingly, while ordering in the hard-sphere systems is very difficult to model[271,272] ordering transitions of apparently more complex hard rods (specifically, spherocylinders) were treated analytically by Lars Onsager some fifty years ago.[264]

For hard rods in a sufficiently dilute solution, the entropy is maximized when the rods are free to take on any orientation and position – this is the isotropic phase. As the solution becomes more concentrated, the rods become both translationally and rotationally constrained in such a way that the freedom to rotate restricts the freedom to translate and vice versa. In doing so, the total entropy becomes maximal when the rods sacrifice some of their orientational freedom in exchange for increasing translational freedom. As depicted in Figure 17a, the relative orientation between rods can make a dramatic difference in the total excluded volume; consequently, there is a significant entropic gain associated with the mutual orientation of rods at sufficiently high volume fractions.

This qualitative description is validated by rigorous statistical mechanical arguments. For a canonical ensemble of hard-rods, the Helmholtz free-energy, F, is related to the canonical partition function, Q, as $F = -kT \ln Q$, from which the pressure may be derived as $P = -(\partial F/\partial V)_T$. Expanding the pressure in a power series of the number density, $\rho = N/V$, and integrating with respect to volume yields

$$F = kTN(-\ln(\rho) + B_2\rho + (1/2)B_3\rho^2 + \ldots) \quad (46)$$

While this expression for the free energy is completely general, it is only useful if it can be shown that the so-called virial coefficients ($B_2, B_3, B_4, \ldots$) become negligible at high orders of expansion. The key difference between systems of hard-spheres (and cubes or plates, for that matter) and that of hard rods is that the virial coefficients of the former are all of the same order.[264] In sharp contrast, the third and higher-order virial coefficients of the hard-rod fluid vanish as the rods become increasingly narrow (i.e., $B_{\geq 3} = 0$ for $h/a \to \infty$).[264]

Using the so-called cluster integrals,[71,264] the second virial coefficients can be calculated directly to give

$$B_2 = -(1/2)v_{exl} = 2h^2D\sin\theta + 2\pi D^2h + (4/3)\pi D^3 \quad (47)$$

where $D = 2a$ is the diameter of the spherocylinder, and h is its length (more specifically, the distance between the hemispherical caps, cf. Figure 17). For large aspect ratios h/D,

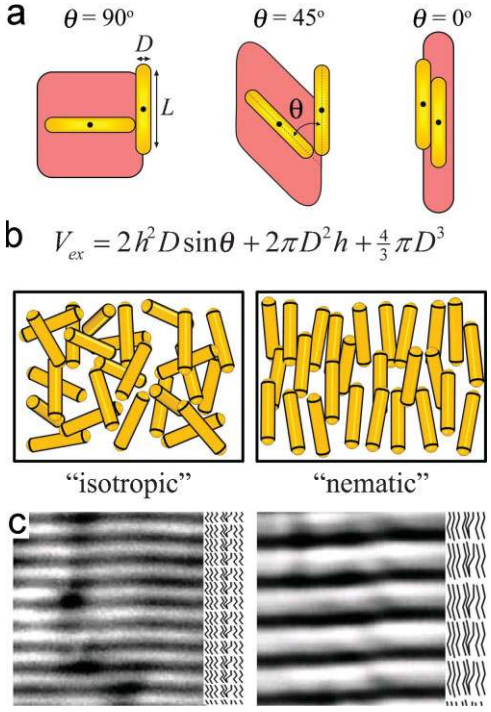

Figure 17. Excluded volume between hard rods (so-called spherocylinders) and the isotropic-nematic phase transition. In a dilute solution of hard rods, the free energy of the system depends entirely on the degrees of freedom (translational and rotational) available to the rods. The degrees of freedom available to any one rod, however, depend on the position and orientation of all of the others. If the positions are assumed to be uniformly distributed, then the degrees of freedom per rod depend only on the density and relative orientation between rods. Three relative orientations (a) are shown along with a red-shaded area corresponding to the volume of space excluded to other rods (centers-of-mass indicated by black dots). For rods with high aspect ratios, the excluded volume is significantly reduced when they are parallel. b) When the density of rods is sufficiently high, the desire for the system to maximize the space available to each rod – and hence the entropy of the system – results in the macroscopically observable phase transition from the isotropic into a nematic phase (where all rods become parallel with respect to each other). c) Smectic phases formed by mutants of the *fd* virus of different length (0.64 μm, left; 1.2 μm, right) at high volume fractions. Reprinted from Reference [277].

equation (47) simplifies to $B_2 \approx -h^2 D \sin\theta$, and all higher-order coefficients are negligibly small. With this simplification and following the reasoning detailed in Reference [264], the free energy becomes

$$F = \frac{\pi}{4} kTh^2 D\left(\rho \ln\left(\frac{\pi}{4} h^2 D\rho\right) + \sigma(\alpha)\rho + \xi(\alpha)\frac{\pi}{4} h^2 D\rho^2\right)$$
$$\text{with} \quad \sigma(\alpha) = \ln\left(\frac{\alpha\cosh(\alpha)}{4\pi\sinh(\alpha)}\right) - 1 + \frac{\arctan(e^{\alpha}) - \arctan(e^{-\alpha})}{\sinh(a)}$$
$$\text{and} \quad \xi(\alpha) = \frac{2I_2(\alpha)}{\sinh^2(\alpha)} \tag{48}$$

Here, $I_2()$ is the modified Bessel function of the first kind, and α has the meaning of an order parameter – i.e., when it is nearly zero, the orientations of the rods are random; when it is large, the rods are highly oriented. Importantly, the free energy is found to be unstable with respect to orientational fluctuations in the case of an isotropic distribution when the density exceeds $\rho_c = 1/(\pi h^2 D)$, at which point a phase transition occurs, and the rods orient to form the so-called nematic phase. Although more challenging to describe theoretically, another well-known phase transition is observed empirically at even higher densities – namely, the nematic-to-smectic transition (see Figure 17c for experimental images).

In general, entropic ordering effects will *always* favor the formation of order structures from of monodisperse particles at sufficiently high volume fractions *provided* that the system remains ergodic.[77] As seen in Section 2.3, this ergodic criterion may be difficult to achieve at the highest volume fractions; however, nanoscale systems are particularly well suited for this challenge, as they rapidly sample their accessible phase space.[273] These effects are often encountered (although not always acknowledged) in nanoparticle systems during the evaporation of the surrounding solvent. Provided this process occurs quasistatically (i.e., sufficiently slowly as to maintain equilibrium), the volume fraction of nanoparticles increases steadily with decreasing solvent volume until they crystallize at a critical volume fraction determined by the shapes of the particles. Further evaporation of the solvent ultimately "freezes" the particles in a close-packed geometry, for which the system is no longer ergodic but retains the order induced by entropic crystallization.

For the practicing nanoscientist, these purely entropic effects can be combined with additional attractive interactions to yield a rich variety of minimal free-energy structures. For example, oppositely charged particles in dilute solutions may assemble into a NaCl lattice to minimize the potential energy of the system. In contrast, uncharged particles crystallize into close-packed fcc structures at sufficiently high volume fractions via entropic ordering. By varying the magnitude of the electrostatic interactions, competition between energetic and entropic ordering may result in a range of structures distinct from these limiting scenarios.[274] Indeed, the combination of electrostatic and vdW interactions with entropic ordering in binary nanoparticle mixtures can lead to at least 15 possible crystal structures depending on the relative magnitudes of these competing effects.[62,275] It is probably with such multiple-interaction systems such as this one, where the full potential of self-assembly can be harnessed to tailor the nanostructured materials of the future.

Table 1. Interaction potentials.

Interaction Type	Geometry	Formula	Range
Any	Spherical particles	$U_{DA}(L) \approx \frac{2\pi a_1 a_2}{(a_1+a_2)} \int_h^{\infty} U_{FP}(z)dz$	$L \ll \frac{a_1 a_2}{a_1+a_2}$
Van der Waals	Spherical particles	$U_{vdW}(r) = \frac{A}{3}\left[\frac{a_1 a_2}{r^2-(a_1+a_2)^2} + \frac{a_1 a_2}{r^2-(a_1-a_2)^2} + \frac{1}{2}\ln\left(\frac{r^2-(a_1+a_2)^2}{r^2-(a_1-a_2)^2}\right)\right]$	all r
Van der Waals	Spherical particles	$U_{vdW} \approx -Aa/24L$	$L \ll a$
Van der Waals	Flat plates	$U_{Ham} = -A/12\pi L^2$	all L
Van der Waals	Cylinders side by side	$U_{Ham} = -Aha^{1/2}/24L^{3/2}$	$L \ll a$
Van der Waals	Cylinders end to end	$U_{Ham} = -\frac{Aa^2}{12}\left(\frac{1}{L^2} - \frac{1}{(L+h)^2} - \frac{2}{(L+2h)^2}\right)$	$L \ll a$
Electrostatic	Sphere-like particles	$U_{es} = \frac{Q_1^{\infty} Q_2^{\infty}}{4\pi\varepsilon_0\varepsilon(1+\kappa a_1)(1+\kappa a_2)} \frac{\exp[-\kappa(r-a_1-a_2)]}{r}$	$r \gg \kappa^{-1}$
Magnetic dipole–dipole	Spherical particles	$U_{dd} = \frac{\mathbf{m}_1\cdot\mathbf{m}_2 - 3(\mathbf{m}_1\cdot\hat{\mathbf{r}})(\mathbf{m}_2\cdot\hat{\mathbf{r}})}{4\pi\mu_0 r^3}$	all r
Fluctuating dipole–dipole	Spherical particles	$U_{dd}(r) = \frac{-1}{3kT}\left(\frac{m_1 m_2}{4\pi\mu_0 r^3}\right)^2$	$\frac{m_1 m_2}{2\pi\mu_0 r^3} \ll 6kT$
DNA bridging	Spherical particles	$U_{dna}(L) \approx -\frac{kT\Gamma^2 c_l}{c_0^2}\exp\left(\frac{-\Delta G}{kT}\right)\frac{(2h-L)^2}{h^2}$	$L < h < 2L$
Crosslinking	Spherical particles	$U_c = \frac{\pi a_1 a_2 \lambda}{(a_1+a_2)}\Gamma kT \ln\left(\frac{[1+x\exp(-\Delta\mu_1^0/kT)]^2}{1+x\exp(-2\Delta\mu_1^0/kT)}\right)$	At contact
Steric repulsion	Spherical particles	$U_S(u) \approx \frac{2\pi a_1 a_2}{(a_1+a_2)}\frac{\pi^2 kT\Gamma L_0^3}{6Nb^2}\left[-\ln u - \frac{9}{5}(1-u) + \frac{1}{3}(1-u^3) - \frac{1}{3}(1-u^6)\right]$	$L_h \ll a$
Depletion	Spherical particles	$U_{dep}(r) = -\frac{\pi p_0}{12}[2(2a+\sigma)^3 - 3(2a+\sigma)^2 r + r^3]$	$r < 2a+\sigma$

NANO MICRO small

8. Conclusions and Outlook

In summary, the examples covered in this Review illustrate the multitude of forces acting between nanoscopic components and underlying their self-assembly into larger structures. While there is certainly more fundamental work to be done to characterize these interactions – both experimentally and theoretically – the practical challenge of nanoscience is to apply these interactions in self-assembly of new, nanostructured materials. Currently, the formation of most assemblies can be modeled and justified only a posteriori, and there are few examples of systems in which the course of nanoscale self-assembly was predicted a priori from the knowledge of individual interactions. There are at least two reasons for this: i) Models for various interparticle potentials are inaccurate or inappropriately used or ii) exploring the consequences of even accurate models for large numbers of nanocomponents remains beyond the currently available computational resources. We hope this Review can help with the first of these issues by systematizing and cataloguing (see Table 1) interparticle potentials that are most appropriate for the nanoscale. Incorporation of these potentials into efficient simulations algorithms appears the next logical step en route to the rational engineering of nanoscale self-assembly.

Keywords:
electrostatics · entropy · nanoparticles · nanoscale forces · self-assembly

[1] J. Park, J. Joo, S. G. Kwon, Y. Jang, T. Hyeon, *Angew. Chem. Int. Ed.* **2007**, *46*, 4630–4660.
[2] W. Q. Han, S. S. Fan, Q. Q. Li, Y. D. Hu, *Science* **1997**, *277*, 1287–1289.
[3] H. J. Dai, E. W. Wong, Y. Z. Lu, S. S. Fan, C. M. Lieber, *Nature* **1995**, *375*, 769–772.
[4] L. Vayssieres, *Adv. Mater.* **2003**, *15*, 464–466.
[5] B. Nikoobakht, M. A. El-Sayed, *Chem. Mater.* **2003**, *15*, 1957–1962.
[6] B. J. Wiley, Y. C. Chen, J. M. McLellan, Y. J. Xiong, Z. Y. Li, D. Ginger, Y. N. Xia, *Nano Lett.* **2007**, *7*, 1032–1036.
[7] R. Klajn, A. O. Pinchuk, G. C. Schatz, B. A. Grzybowski, *Angew. Chem. Int. Ed.* **2007**, *46*, 8363–8367.
[8] C. X. Kan, X. G. Zhu, G. H. Wang, *J. Phys. Chem. B* **2006**, *110*, 4651–4656.
[9] J. E. Millstone, G. S. Metraux, C. A. Mirkin, *Adv. Funct. Mater.* **2006**, *16*, 1209–1214.
[10] S. H. Chen, Z. Y. Fan, D. L. Carroll, *J. Phys. Chem. B* **2002**, *106*, 10777–10781.
[11] L. Manna, E. C. Scher, A. P. Alivisatos, *J. Am. Chem. Soc.* **2000**, *122*, 12700–12706.
[12] L. Fang, J. Y. Park, Y. Cui, P. Alivisatos, J. Shcrier, B. Lee, L. W. Wang, M. Salmeron, *J. Chem. Phys.* **2007**, *127*, 184704.
[13] M. C. Daniel, D. Astruc, *Chem. Rev.* **2004**, *104*, 293–346.
[14] S. J. Oldenburg, R. D. Averitt, S. L. Westcott, N. J. Halas, *Chem. Phys. Lett.* **1998**, *288*, 243–247.
[15] F. Caruso, R. A. Caruso, H. Mohwald, *Science* **1998**, *282*, 1111–1114.
[16] Y. D. Yin, R. M. Rioux, C. K. Erdonmez, S. Hughes, G. A. Somorjai, A. P. Alivisatos, *Science* **2004**, *304*, 711–714.
[17] J. Y. Chen, B. Wiley, Z. Y. Li, D. Campbell, F. Saeki, H. Cang, L. Au, J. Lee, X. D. Li, Y. N. Xia, *Adv. Mater.* **2005**, *17*, 2255–2261.
[18] X. M. Lu, L. Au, J. McLellan, Z. Y. Li, M. Marquez, Y. N. Xia, *Nano Lett.* **2007**, *7*, 1764–1769.
[19] S. E. Skrabalak, J. Y. Chen, Y. G. Sun, X. M. Lu, L. Au, C. M. Cobley, Y. N. Xia, *Accounts Chem. Res.* **2008**, *41*, 1587–1595.
[20] Y. H. Wei, R. Klajn, A. O. Pinchuk, B. A. Grzybowski, *Small* **2008**, *4*, 1635–1639.
[21] T. Teranishi, Y. Inoue, M. Nakaya, Y. Oumi, T. Sano, *J. Am. Chem. Soc.* **2004**, *126*, 9914–9915.
[22] W. L. Shi, H. Zeng, Y. Sahoo, T. Y. Ohulchanskyy, Y. Ding, Z. L. Wang, M. Swihart, P. N. Prasad, *Nano Lett.* **2006**, *6*, 875–881.
[23] M. Brust, M. Walker, D. Bethell, D. J. Schiffrin, R. Whyman, *J. Chem. Soc, Chem. Commun.* **1994**, 801–802.
[24] Y. G. Sun, Y. N. Xia, *Science* **2002**, *298*, 2176–2179.
[25] S. H. Sun, C. B. Murray, D. Weller, L. Folks, A. Moser, *Science* **2000**, *287*, 1989–1992.
[26] T. S. Ahmadi, Z. L. Wang, T. C. Green, A. Henglein, M. A. ElSayed, *Science* **1996**, *272*, 1924–1926.
[27] T. Trindade, P. O'Brien, N. L. Pickett, *Chem. Mat.* **2001**, *13*, 3843–3858.
[28] M. Bruchez, M. Moronne, P. Gin, S. Weiss, A. P. Alivisatos, *Science* **1998**, *281*, 2013–2016.
[29] E. A. Meulenkamp, *J. Phys. Chem. B* **1998**, *102*, 5566–5572.
[30] S. H. Sun, H. Zeng, *J. Am. Chem. Soc.* **2002**, *124*, 8204–8205.
[31] S. Vaucher, M. Li, S. Mann, *Angew. Chem. Int. Edit.* **2000**, *39*, 1793–1796.
[32] C. B. Murray, C. R. Kagan, M. G. Bawendi, *Annu. Rev. Mater. Sci.* **2000**, *30*, 545–610.
[33] R. Gref, Y. Minamitake, M. T. Peracchia, V. Trubetskoy, V. Torchilin, R. Langer, *Science* **1994**, *263*, 1600–1603.
[34] C. R. Martin, *Science* **1994**, *266*, 1961–1966.
[35] J. B. Broderick, M. J. Natan, T. V. Ohalloran, R. P. Vanduyne, *Biochemistry* **1993**, *32*, 13771–13776.
[36] C. M. McIntosh, E. A. Esposito, A. K. Boal, J. M. Simard, C. T. Martin, V. M. Rotello, *J. Amer. Chem. Soc.* **2001**, *123*, 7626–7629.
[37] E. Katz, I. Willner, *Angew. Chem. Int. Ed.* **2004**, *43*, 6042–6108.
[38] M. Zheng, F. Davidson, X. Huang, *J. Amer. Chem. Soc.* **2003**, *125*, 7790–7791.
[39] A. M. Kalsin, M. Fialkowski, M. Paszewski, S. K. Smoukov, K. J. M. Bishop, B. A. Grzybowski, *Science* **2006**, *312*, 420–424.
[40] A. M. Kalsin, B. A. Grzybowski, *Nano Lett.* **2007**, *7*, 1018–1021.
[41] A. M. Kalsin, B. Kowalczyk, S. K. Smoukov, R. Klajn, B. A. Grzybowski, *J. Am. Chem. Soc.* **2006**, *128*, 15046–15047.
[42] T. G. Drummond, M. G. Hill, J. K. Barton, *Nat. Biotechnol.* **2003**, *21*, 1192–1199.
[43] S. W. Chen, R. S. Ingram, M. J. Hostetler, J. J. Pietron, R. W. Murray, T. G. Schaaff, J. T. Khoury, M. M. Alvarez, R. L. Whetten, *Science* **1998**, *280*, 2098–2101.
[44] D. I. Gittins, D. Bethell, D. J. Schiffrin, R. J. Nichols, *Nature* **2000**, *408*, 67–69.
[45] Y. Jin, W. Lu, J. Q. Hu, X. Yao, J. H. Li, *Electrochem. Commun.* **2007**, *9*, 1086–1090.
[46] J. F. Sargent, *Nanotechnology: A Policy Primer*, CRS Report for Congress, 2008.
[47] M. Y. Han, X. H. Gao, J. Z. Su, S. Nie, *Nat. Biotechnol.* **2001**, *19*, 631–635.
[48] M. M. C. Cheng, G. Cuda, Y. L. Bunimovich, M. Gaspari, J. R. Heath, H. D. Hill, C. A. Mirkin, A. J. Nijdam, R. Terracciano, T. Thundat, M. Ferrari, *Curr. Opin. Chem. Biol.* **2006**, *10*, 11–19.
[49] Z. Wang, J. Lee, A. R. Cossins, M. Brust, *Anal. Chem.* **2005**, *77*, 5770–5774.
[50] M. Ferrari, *Nat. Nanotechnol.* **2008**, *3*, 131–132.
[51] M. Ferrari, *Nat. Rev. Cancer* **2005**, *5*, 161–171.
[52] K. Kneipp, H. Kneipp, I. Itzkan, R. R. Dasari, M. S. Feld, *Chem. Rev.* **1999**, *99*, 2957–2976.
[53] S. J. Tans, A. R. M. Verschueren, C. Dekker, *Nature* **1998**, *393*, 49–52.
[54] Y. Cui, C. M. Lieber, *Science* **2001**, *291*, 851–853.

[55] C. P. Collier, T. Vossmeyer, J. R. Heath, *Annu. Rev. Phys. Chem.* **1998**, *49*, 371–404.
[56] G. M. Whitesides, B. Grzybowski, *Science* **2002**, *295*, 2418–2421.
[57] M. Fialkowski, K. J. M. Bishop, R. Klajn, S. K. Smoukov, C. J. Campbell, B. A. Grzybowski, *J. Phys. Chem. B* **2006**, *110*, 2482–2496.
[58] J. M. Nam, C. S. Thaxton, C. A. Mirkin, *Science* **2003**, *301*, 1884–1886.
[59] H. Yan, S. H. Park, G. Finkelstein, J. H. Reif, T. H. LaBean, *Science* **2003**, *301*, 1882–1884.
[60] S. Hecht, *Small* **2005**, *1*, 26–29.
[61] M. Dorogi, J. Gomez, R. Osifchin, R. P. Andres, R. Reifenberger, *Phys. Rev. B* **1995**, *52*, 9071–9077.
[62] E. V. Shevchenko, D. V. Talapin, N. A. Kotov, S. O'Brien, C. B. Murray, *Nature* **2006**, *439*, 55–59.
[63] R. Klajn, K. J. M. Bishop, M. Fialkowski, M. Paszewski, C. J. Campbell, T. P. Gray, B. A. Grzybowski, *Science* **2007**, *316*, 261–264.
[64] L. Zhou, W. J. Wen, P. Sheng, *Phys. Rev. Lett.* **1998**, *81*, 1509–1512.
[65] J. N. Israelachvili, *Intermolecular and Surface Forces*, Academic Press, New York **1991**.
[66] W. B. Russel, D. A. Saville, W. R. Schowalter, *Colloidal Dispersions*, Cambridge University Press, Cambridge, UK **1989**.
[67] Y. J. Min, M. Akbulut, K. Kristiansen, Y. Golan, J. Israelachvili, *Nat. Mater.* **2008**, *7*, 527–538.
[68] D. Henderson, D. M. Duh, X. L. Chu, D. Wasan, *J. Colloid Interface Sci.* **1997**, *185*, 265–268.
[69] B. V. Deryaguin, *Kolloid Z.* **1934**, *69*, 155.
[70] L. R. White, *J. Colloid Interface Sci.* **1983**, *95*, 286–288.
[71] T. L. Hill, *Statistical Mechanics: Principles and Selected Applications*, Dover, New York **1987**.
[72] N. E. Chayen, *Trends Biotechnol.* **2002**, *20*, 98–98.
[73] S. D. Durbin, G. Feher, *Annu. Rev. Phys. Chem.* **1996**, *47*, 171–204.
[74] K. A. Dawson, *Curr. Opin. Colloid Interface Sci.* **2002**, *7*, 218–227.
[75] G. Foffi, G. D. McCullagh, A. Lawlor, E. Zaccarelli, K. A. Dawson, F. Sciortino, P. Tartaglia, D. Pini, G. Stell, *Phys. Rev. E* **2002**, *65*, 031407.
[76] F. Sciortino, P. Tartaglia, *Adv. Phys.* **2005**, *54*, 471–524.
[77] J. L. Lebowitz, O. Penrose, *Phys. Today* **1973**, *26*, 23–29.
[78] M. Muschol, F. Rosenberger, *J. Chem. Phys.* **1997**, *107*, 1953–1962.
[79] S. A. Harfenist, Z. L. Wang, M. M. Alvarez, I. Vezmar, R. L. Whetten, *J. Phys. Chem.* **1996**, *100*, 13904–13910.
[80] C. B. Murray, C. R. Kagan, M. G. Bawendi, *Science* **1995**, *270*, 1335–1338.
[81] T. K. Sau, C. J. Murphy, *Langmuir* **2005**, *21*, 2923–2929.
[82] N. R. Jana, *Angew. Chem. Int. Ed.* **2004**, *43*, 1536–1540.
[83] A. D. McLachlan, *Proc. R. Soc. London Ser. A* **1963**, *274*, 80–90.
[84] A. D. McLachlan, *Proc. R. Soc. London Ser. A* **1963**, *271*, 387–401.
[85] H. C. Hamaker, *Physica* **1937**, *4*, 1058–1072.
[86] I. E. Dzyaloshinskii, E. M. Lifshitz, L. P. Pitaevskii, *Adv. Phys.* **1961**, *10*, 165–209.
[87] V. A. Parsegian, *Van der Waals Forces*, Cambridge University Press, Cambridge, UK **2006**.
[88] H. Y. Kim, J. O. Sofo, D. Velegol, M. W. Cole, A. A. Lucas, *J. Chem. Phys.* **2006**, *124*, 074504.
[89] H. Y. Kim, J. O. Sofo, D. Velegol, M. W. Cole, A. A. Lucas, *Langmuir* **2007**, *23*, 1735–1740.
[90] S. W. Lee, W. M. Sigmund, *Colloid Surf. A–Physicochem. Eng. Asp.* **2002**, *204*, 43–50.
[91] A. Milling, P. Mulvaney, I. Larson, *J. Colloid Interface Sci.* **1996**, *180*, 460–465.
[92] Estimating Hamaker coefficients through the Hamaker integral approximation, that is, as $A=C_{vdW}\pi^2/\nu_1\nu_2$, is often as impractical as it is inaccurate (neglecting many-body effects), because it requires knowledge of the parameter C_{vdW} characterizing pairwise interactions between atoms/molecules in the gas phase: consider the case of gold described in the text.
[93] V. A. Parsegian, G. H. Weiss, *J. Colloid Interface Sci.* **1981**, *81*, 285–289.
[94] D. Langbein, *J. Phys. Chem. Solids* **1971**, *32*, 1657–1667.
[95] Y. Lalatonne, J. Richardi, M. P. Pileni, *Nat. Mater.* **2004**, *3*, 121–125.
[96] R. L. Whetten, J. T. Khoury, M. M. Alvarez, S. Murthy, I. Vezmar, Z. L. Wang, P. W. Stephens, C. L. Cleveland, W. D. Luedtke, U. Landman, *Adv. Mater.* **1996**, *8*, 428–&.
[97] C. Noguez, *J. Phys. Chem. C* **2007**, *111*, 3806–3819.
[98] A. A. Lucas, *Physica* **1968**, *39*, 5–12.
[99] M. J. Renne, B. R. A. Nijboer, *Chem. Phys. Lett.* **1967**, *1*, 317–320.
[100] The failure of the Hamaker integral approximation at large separations originates from the use of Hamaker coefficients derived from the continuum DLP theory for flat plates. These coefficients incorporate many-body effects, which are absent at large separations (cf. Reference [89]).
[101] Y. K. Park, S. H. Yoo, S. Park, *Langmuir* **2007**, *23*, 10505–10510.
[102] L. Motte, F. Billoudet, M. P. Pileni, *J. Phys. Chem.* **1995**, *99*, 16425–16429.
[103] B. A. Korgel, S. Fullam, S. Connolly, D. Fitzmaurice, *J. Phys. Chem. B* **1998**, *102*, 8379–8388.
[104] P. C. Ohara, D. V. Leff, J. R. Heath, W. M. Gelbart, *Phys. Rev. Lett.* **1995**, *75*, 3466–3469.
[105] S. Murthy, Z. L. Wang, R. L. Whetten, *Philos. Mag. Lett.* **1997**, *75*, 321–327.
[106] K. J. Klabunde, C. M. Sorensen, X. M. Lin, *J. Nanopart. Res.* **2000**, *2*, 157–167.
[107] C. B. Murray, D. J. Norris, M. G. Bawendi, *J. Am. Chem. Soc.* **1993**, *115*, 8706–8715.
[108] M. Yamaki, J. Higo, K. Nagayama, *Langmuir* **1995**, *11*, 2975–2978.
[109] M. E. Leunissen, C. G. Christova, A. P. Hynninen, C. P. Royall, A. I. Campbell, A. Imhof, M. Dijkstra, R. van Roij, A. van Blaaderen, *Nature* **2005**, *437*, 235–240.
[110] B. A. Grzybowski, A. Winkleman, J. A. Wiles, Y. Brumer, G. M. Whitesides, *Nat. Mater.* **2003**, *2*, 241–245.
[111] J. Kolny, A. Kornowski, H. Weller, *Nano Lett.* **2002**, *2*, 361–364.
[112] S. K. Smoukov, K. J. M. Bishop, B. Kowalczyk, A. M. Kalsin, B. A. Grzybowski, *J. Am. Chem. Soc.* **2007**, *129*, 15623–15630.
[113] E. C. Hao, B. Yang, J. H. Zhang, X. Zhang, J. Q. Sun, S. C. Shen, *J. Mater. Chem.* **1998**, *8*, 1327–1328.
[114] D. Lee, M. F. Rubner, R. E. Cohen, *Nano Lett.* **2006**, *6*, 2305–2312.
[115] A. N. Shipway, M. Lahav, R. Gabai, I. Willner, *Langmuir* **2000**, *16*, 8789–8795.
[116] L. Hong, A. Cacciuto, E. Luijten, S. Granick, *Nano Lett.* **2006**, *6*, 2510–2514.
[117] A. Ghezelbash, B. Koo, B. A. Korgel, *Nano Lett.* **2006**, *6*, 1832–1836.
[118] Z. Y. Tang, N. A. Kotov, M. Giersig, *Science* **2002**, *297*, 237–240.
[119] L. Guldbrand, B. Jonsson, H. Wennerstrom, P. Linse, *J. Chem. Phys.* **1984**, *80*, 2221–2228.
[120] Y. Levin, *Rep. Prog. Phys.* **2002**, *65*, 1577–1632.
[121] E. J. W. Verwey, J. T. G. Overbeek, *Theory of the Stability of Lyophobic Colloids*, Dover, New York **1948**.
[122] G. Gouy, **1910**, *9*, 457.
[123] D. L. Chapman, *Phil. Mag.* **1913**, *25*, 475.
[124] P. W. Debye, E. Huckel, *Phys. Z.* **1923**, *24*, 185.
[125] S. L. Carnie, D. Y. C. Chan, J. S. Gunning, *Langmuir* **1994**, *10*, 2993–3009.
[126] D. Y. C. Chan, D. J. Mitchell, *J. Colloid Interface Sci.* **1983**, *95*, 193–197.
[127] S. Alexander, P. M. Chaikin, P. Grant, G. J. Morales, P. Pincus, D. Hone, *J. Chem. Phys.* **1984**, *80*, 5776–5781.

[128] D. McCormack, S. L. Carnie, D. Y. C. Chan, *J. Colloid Interface Sci.* **1995**, *169*, 177–196.
[129] K. J. M. Bishop, B. A. Grzybowski, *ChemPhysChem* **2007**, *8*, 2171–2176.
[130] D. V. Leff, P. C. Ohara, J. R. Heath, W. M. Gelbart, *J. Phys. Chem.* **1995**, *99*, 7036–7041.
[131] D. G. Grier, *J. Phys. Condens. Matter* **2000**, *12*, A85–A94.
[132] A. M. Kalsin, B. Kowalczyk, P. Wesson, M. Paszewski, B. A. Grzybowski, *J. Am. Chem. Soc.* **2007**, *129*, 6664–6665.
[133] K. J. M. Bishop, B. Kowalczyk, B. A. Grzybowski, *J. Phys. Chem. B* **2009**, *113*, 1413–1417.
[134] J. Venermo, A. Sihvola, *J. Electrost.* **2005**, *63*, 101–117.
[135] P. Pramod, S. T. S. Joseph, K. G. Thomas, **2007**, *129*, 6712–6713.
[136] A. Y. Grosberg, T. T. Nguyen, B. I. Shklovskii, *Rev. Mod. Phys.* **2002**, *74*, 329–345.
[137] P. Kekicheff, S. Marcelja, T. J. Senden, V. E. Shubin, *J. Chem. Phys.* **1993**, *99*, 6098–6113.
[138] R. Kjellander, S. Marcelja, R. M. Pashley, J. P. Quirk, *J. Chem. Phys.* **1990**, *92*, 4399–4407.
[139] V. Vlachy, *Annu. Rev. Phys. Chem.* **1999**, *50*, 145–165.
[140] J. P. Hansen, I. R. McDonald, *Theory of Simple Liquids*, Academic Press, New York **1976**.
[141] L. Belloni, *J. Phys. Condensed Matt.* **2000**, *12*, R549–R587.
[142] R. Kjellander, S. Marcelja, *J. Phys. Chem.* **1986**, *90*, 1230–1232.
[143] R. Kjellander, S. Marcelja, J. P. Quirk, *J. Colloid Interface Sci.* **1988**, *126*, 194–211.
[144] R. D. Groot, *J. Chem. Phys.* **1991**, *95*, 9191–9203.
[145] J. P. Valleau, R. Ivkov, G. M. Torrie, *J. Chem. Phys.* **1991**, *95*, 520–532.
[146] S. Engstrom, H. Wennerstrom, *J. Phys. Chem.* **1978**, *82*, 2711–2714.
[147] R. Messina, C. Holm, K. Kremer, *Phys. Rev. E* **2001**, *64*, 14.
[148] J. C. Neu, *Phys. Rev. Lett.* **1999**, *82*, 1072–1074.
[149] J. E. Sader, D. Y. C. Chan, *J. Colloid Interface Sci.* **1999**, *213*, 268–269.
[150] R. Kjellander, S. Marcelja, *Chem. Phys. Lett.* **1984**, *112*, 49–53.
[151] V. A. Bloomfield, *Biopolymers* **1991**, *31*, 1471–1481.
[152] M. O. de la Cruz, L. Belloni, M. Delsanti, J. P. Dalbiez, O. Spalla, M. Drifford, *J. Chem. Phys.* **1995**, *103*, 5781–5791.
[153] J. C. Crocker, D. G. Grier, *Phys. Rev. Lett.* **1994**, *73*, 352–355.
[154] D. Weller, M. F. Doerner, *Annu. Rev. Mater. Sci.* **2000**, *30*, 611–644.
[155] H. Zeng, J. Li, J. P. Liu, Z. L. Wang, S. H. Sun, *Nature* **2002**, *420*, 395–398.
[156] S. H. Sun, *Adv. Mater.* **2006**, *18*, 393–403.
[157] Y. K. Hahn, Z. Jin, J. H. Kang, E. Oh, M. K. Han, H. S. Kim, J. T. Jang, J. H. Lee, J. Cheon, S. H. Kim, H. S. Park, J. K. Park, *Anal. Chem.* **2007**, *79*, 2214–2220.
[158] Q. A. Pankhurst, J. Connolly, S. K. Jones, J. Dobson, *J. Phys. D–Appl. Phys.* **2003**, *36*, R167–R181.
[159] S. K. Pulfer, S. L. Ciccotto, J. M. Gallo, *J. Neuro–Oncol.* **1999**, *41*, 99–105.
[160] R. V. Mehta, R. V. Upadhyay, S. W. Charles, C. N. Ramchand, *Biotechnol. Tech.* **1997**, *11*, 493–496.
[161] R. K. Gilchrist, R. Medal, W. D. Shorey, R. C. Hanselman, J. C. Parrott, C. B. Taylor, *Ann. Surg.* **1957**, *146*, 596–606.
[162] A. Jordan, R. Scholz, P. Wust, H. Fahling, R. Felix, *J. Magn. Magn. Mater.* **1999**, *201*, 413–419.
[163] J. M. Perez, L. Josephson, T. O'Loughlin, D. Hogemann, R. Weissleder, *Nat. Biotechnol.* **2002**, *20*, 816–820.
[164] J. M. Perez, F. J. Simeone, Y. Saeki, L. Josephson, R. Weissleder, *J. Am. Chem. Soc.* **2003**, *125*, 10192–10193.
[165] J. R. Thomas, *J. Appl. Phys.* **1966**, *37*, 2914–2915.
[166] M. Tanase, L. A. Bauer, A. Hultgren, D. M. Silevitch, L. Sun, D. H. Reich, P. C. Searson, G. J. Meyer, *Nano Lett.* **2001**, *1*, 155–158.
[167] H. L. Niu, Q. W. Chen, H. F. Zhu, Y. S. Lin, X. Zhang, *J. Mater. Chem.* **2003**, *13*, 1803–1805.
[168] M. Tanase, D. M. Silevitch, A. Hultgren, L. A. Bauer, P. C. Searson, G. J. Meyer, D. H. Reich, *J. Appl. Phys.* **2001**, *91*, 8549–8551.
[169] S. L. Tripp, S. V. Pusztay, A. E. Ribbe, A. Wei, *J. Am. Chem. Soc.* **2002**, *124*, 7914–7915.
[170] S. L. Tripp, R. E. Dunin-Borkowski, A. Wei, *Angew. Chem. Int. Ed.* **2003**, *42*, 5591–5593.
[171] U. Wiedwald, M. Spasova, M. Farle, M. Hilgendorff, M. Giersig, *J. Vac. Sci. Technol. A* **2000**, 1773–1776.
[172] M. Hilgendorff, B. Tesche, M. Giersig, *Aust. J. Chem.* **2001**, *54*, 497–501.
[173] S. H. Sun, C. B. Murray, *IEEE Trans. Magn.* **1998**, *38*, 4325–4330.
[174] M. P. Pileni, *J. Phys. Chem. B* **2001**, *105*, 3358–3371.
[175] G. J. Cheng, D. Romero, G. T. Fraser, A. R. H. Walker, *Langmuir* **2005**, *21*, 12055–12059.
[176] A. Ahniyaz, Y. Sakamoto, L. Bergstrom, *Proc. Natl. Acad. Sci. USA* **2007**, *104*, 17570–17574.
[177] T. Hyeon, *Chem. Commun.* **2003**, 927–934.
[178] J. Park, E. Lee, N. M. Hwang, M. S. Kang, S. C. Kim, Y. Hwang, J. G. Park, H. J. Noh, J. Y. Kini, J. H. Park, T. Hyeon, *Angew. Chem. Int. Ed.* **2005**, *44*, 2872–2877.
[179] S. J. Park, S. Kim, S. Lee, Z. G. Khim, K. Char, T. Hyeon, *J. Am. Chem. Soc.* **2000**, *122*, 8581–8582.
[180] V. F. Puntes, K. M. Krishnan, A. P. Alivisatos, *Science* **2001**, *291*, 2115–2117.
[181] T. Fried, G. Shemer, G. Markovich, *Adv. Mater.* **2001**, *13*, 1158.
[182] T. Hyeon, S. S. Lee, J. Park, Y. Chung, H. Bin Na, *J. Am. Chem. Soc.* **2001**, *123*, 12798–12801.
[183] M. Chen, J. P. Liu, S. H. Sun, *J. Am. Chem. Soc.* **2004**, *126*, 8394–8395.
[184] Y. F. Han, F. X. Chen, Z. Y. Zhong, K. Ramesh, L. W. Chen, E. Widjaja, *J. Phys. Chem. B* **2006**, *110*, 24450–24456.
[185] R. Blakemore, *Science* **1975**, *190*, 377–379.
[186] S. H. Kilcoyne, R. Cywinski, *J. Magn. Magn. Mater.* **1995**, *140*, 1466–1467.
[187] C. Kittel, *Introduction to Solid-State Physics*, Wiley, New York **1996**.
[188] C. Kittel, *Phys. Rev.* **1946**, *70*, 965–971.
[189] C. Kittel, *Rev. Mod. Phys.* **1949**, *21*, 541–584.
[190] J. R. Choi, S. J. Oh, H. Ju, J. Cheon, *Nano Lett.* **2005**, *5*, 2179–2183.
[191] X. Batlle, A. Labarta, *J. Phys. D–Appl. Phys.* **2002**, *35*, R15–R42.
[192] T. K. McNab, R. A. Fox, A. J. F. Boyle, *J. Appl. Phys.* **1968**, *39*, 5703–5711.
[193] K. Abe, Y. Miyamoto, S. Chikazumi, *J. Phys. Soc. Jpn.* **1976**, *41*, 1894–1902.
[194] Y. W. Jun, J. W. Seo, A. Cheon, *Accounts Chem. Res.* **2008**, *41*, 179–189.
[195] M. P. Morales, S. Veintemillas-Verdaguer, M. I. Montero, C. J. Serna, A. Roig, L. Casas, B. Martinez, F. Sandiumenge, *Chem. Mat.* **1999**, *11*, 3058–3064.
[196] S. Linderoth, P. V. Hendriksen, F. Bodker, S. Wells, K. Davies, S. W. Charles, S. Morup, *J. Appl. Phys.* **1994**, *75*, 6583–6585.
[197] V. Sepelak, D. Baabe, D. Mienert, D. Schultze, F. Krumeich, F. J. Litterst, K. D. Becker, *J. Magn. Magn. Mater.* **2003**, *257*, 377–386.
[198] P. C. Scholten, D. L. A. Tjaden, *J. Colloid Interface Sci.* **1980**, *73*, 254–255.
[199] N. Mikuszeit, E. Y. Vedmedenko, H. P. Oepen, *J. Phys. Condensed Matt* **2004**, *16*, 9037–9045.
[200] C. Hattig, B. A. Hess, *Mol. Phys.* **1994**, *81*, 813–824.
[201] S. L. Price, A. J. Stone, M. Alderton, *Mol. Phys.* **1984**, *52*, 987–1001.
[202] A. Goyal, C. K. Hall, O. D. Velev, *Phys. Rev. E* **2008**, *77*, 031401.
[203] R. W. Chantrell, A. Bradbury, J. Popplewell, S. W. Charles, *J. Appl. Phys.* **1982**, *53*, 2742–2744.
[204] J. M. Tavares, J. J. Weis, M. M. T. da Gama, *Phys. Rev. E* **1999**, *59*, 4388–4395.

[205] K. Butter, P. H. H. Bomans, P. M. Frederik, G. J. Vroege, A. P. Philipse, *Nat. Mater.* **2003**, *2*, 88–91.
[206] T. Tlusty, S. A. Safran, *Science* **2000**, *290*, 1328–1331.
[207] A. P. Hynninen, M. Dijkstra, *Phys. Rev. Lett.* **2005**, *94*, 138303.
[208] E. A. Peterson, D. A. Krueger, *J. Colloid Interface Sci.* **1977**, *62*, 24–34.
[209] D. J. Klingenberg, *Aiche J.* **2001**, *47*, 246–249.
[210] S. Singamaneni, V. Bliznyuk, *Appl. Phys. Lett.* **2005**, *87*, 3.
[211] G. R. Desiraju, *Angew. Chem. Int. Ed.* **1995**, *34*, 2311–2327.
[212] B. Moulton, M. J. Zaworotko, *Chem. Rev.* **2001**, *101*, 1629–1658.
[213] J. M. Lehn, *Angew. Chem. Int. Ed.* **1990**, *29*, 1304–1319.
[214] D. Philp, J. F. Stoddart, *Angew. Chem. Int. Ed.* **1996**, *35*, 1155–1196.
[215] X. G. Hu, W. L. Cheng, T. Wang, E. K. Wang, S. J. Dong, *Nanotechnology* **2005**, *16*, 2164–2169.
[216] K. G. Thomas, S. Barazzouk, B. I. Ipe, S. T. S. Joseph, P. V. Kamat, *J. Phys. Chem. B* **2004**, *108*, 13066–13068.
[217] A. P. Alivisatos, K. P. Johnsson, X. Peng, T. E. Wilson, C. J. Loweth, M. P. Bruchez, P. G. Schultz, *Nature* **1996**, *382*, 609–611.
[218] C. A. Mirkin, R. L. Letsinger, R. C. Mucic, J. J. Storhoff, *Nature* **1996**, *382*, 607–609.
[219] Hydrogen bonds can have significant covalent character when the difference in pK_a values of the two electronegative atoms are very similar, resulting in very strong bonds such as those of O–H–O, N–H–N, F–H–F, and other homonuclear bonds. For dissimilar pK_a values, the bond is either a moderately strong hydrogen bond X–H···Y or and ionic one $X^{-}\cdots H\text{–}Y^{+}$, both of which are predominately electrostatic. See Reference [220] and references therein.
[220] T. Steiner, *Angew. Chem. Int. Ed.* **2002**, *41*, 48–76.
[221] S. R. Johnson, S. D. Evans, R. Brydson, *Langmuir* **1998**, *14*, 6639–6647.
[222] L. Cusack, R. Rizza, A. Gorelov, D. Fitzmaurice, *Angew. Chem. Int. Ed.* **1997**, *36*, 848–851.
[223] M. Kimura, S. Kobayashi, T. Kuroda, K. Hanabusa, H. Shirai, *Adv. Mater.* **2004**, *16*, 335–+.
[224] A. K. Boal, F. Ilhan, J. E. DeRouchey, T. Thurn-Albrecht, T. P. Russell, V. M. Rotello, *Nature* **2000**, *404*, 746–748.
[225] Z. H. Sun, W. H. Ni, Z. Yang, X. S. Kou, L. Li, J. F. Wang, *Small* **2008**, *4*, 1287–1292.
[226] J. Huskens, A. Mulder, T. Auletta, C. A. Nijhuis, M. J. W. Ludden, D. N. Reinhoudt, *J. Am. Chem. Soc.* **2004**, *126*, 6784–6797.
[227] J. D. Badjic, A. Nelson, S. J. Cantrill, W. B. Turnbull, J. F. Stoddart, *Accounts Chem. Res.* **2005**, *38*, 723–732.
[228] G. Ercolani, *J. Am. Chem. Soc.* **2003**, *125*, 16097–16103.
[229] W. Rychlik, R. E. Rhoads, *Nucl. Acids Res.* **1989**, *17*, 8543–8551.
[230] A. Csaki, L. Ch, A. Steinbruck, A. Wolff, W. Fritzsche, *International Symposium on DNA–Based Nanodevices. AIP Conference Proceedings* **2008**, *1062*, 49–57.
[231] E. Braun, Y. Eichen, U. Sivan, G. Ben-Yoseph, *Nature* **1998**, *391*, 775–778.
[232] S. Pruneanu, S. A. F. Al-Said, L. Q. Dong, T. A. Hollis, M. A. Galindo, N. G. Wright, A. Houlton, B. R. Horrocks, *Adv. Funct. Mater.* **2008**, *18*, 2444–2454.
[233] Y. Shao, Y. D. Jin, S. J. Dong, *Electrochem. Commun.* **2002**, *4*, 773–779.
[234] E. Dujardin, L. B. Hsin, C. R. C. Wang, S. Mann, *Chem. Commun.* **2001**, 1264–1265.
[235] H. Y. Li, S. H. Park, J. H. Reif, T. H. LaBean, H. Yan, *J. Am. Chem. Soc.* **2004**, *126*, 418–419.
[236] J. D. Le, Y. Pinto, N. C. Seeman, K. Musier-Forsyth, T. A. Taton, R. A. Kiehl, *Nano Lett.* **2004**, *4*, 2343–2347.
[237] J. Sharma, R. Chhabra, A. Cheng, J. Brownell, Y. Liu, H. Yan, *Science* **2009**, *323*, 112–116.
[238] E. M. Puchner, S. K. Kufer, M. Strackharn, S. W. Stahl, H. E. Gaub, *Nano Lett.* **2008**, *8*, 3692–3695.
[239] J. SantaLucia, *Proc. Natl. Acad. Sci. USA* **1998**, *95*, 1460–1465.
[240] D. M. Crothers, B. H. Zimm, *J. Mol. Biol.* **1964**, *9*, 1–&.
[241] P. L. Biancaniello, A. J. Kim, J. C. Crocker, *Phys. Rev. Lett.* **2005**, *94*, 058302.
[242] A. K. Dutt, A. Datta, *J. Phys. Chem. A* **1998**, *102*, 7981–7983.
[243] M. C. Murphy, I. Rasnik, W. Cheng, T. M. Lohman, T. J. Ha, *Biophys. J.* **2004**, *86*, 2530–2537.
[244] D. S. Karpovich, G. J. Blanchard, *Langmuir* **1994**, *10*, 3315–3322.
[245] Y. Wei, K. J. M. Bishop, J. Kim, S. Soh, B. A. Grzybowski, 2009, unpublished results.
[246] S. T. Milner, *Science* **1991**, *251*, 905–914.
[247] E. P. K. Currie, W. Norde, M. A. C. Stuart, *Adv. Colloid Interface Sci.* **2003**, *100*, 205–265.
[248] T. Morinaga, K. Ohno, Y. Tsujii, T. Fukuda, **2008**, *41*, 3620–3626.
[249] P. G. de Gennes, *Adv. Colloid Interface Sci.* **1987**, *27*, 189–209.
[250] J. U. Kim, M. W. Matsen, *Macromolecules* **2008**, *41*, 4435–4443.
[251] S. T. Milner, T. A. Witten, M. E. Cates, *Macromolecules* **1988**, *21*, 2610–2619.
[252] C. M. Wijmans, E. B. Zhulina, *Macromolecules* **1993**, *26*, 7214–7224.
[253] E. Lindberg, C. Elvingson, *J. Chem. Phys.* **2001**, *114*, 6343–6352.
[254] M. Rubenstein, R. H. Colby, *Polymer Physics*, Oxford University Press, Oxford, UK **2003**.
[255] S. T. Milner, *Europhys. Lett.* **1988**, *7*, 695–699.
[256] J. Mewis, W. J. Frith, T. A. Strivens, W. B. Russel, *Aiche J.* **1989**, *35*, 415–422.
[257] U. Genz, B. Daguanno, J. Mewis, R. Klein, *Langmuir* **1994**, *10*, 2206–2212.
[258] S. Asakura, F. Oosawa, *J. Chem. Phys.* **1954**, *22*, 1255.
[259] S. Badaire, C. Cottin-Bizonne, A. D. Stroock, *Langmuir* **2008**, *24*, 11451–11463.
[260] S. Abbas, T. P. Lodge, *Phys. Rev. Lett.* **2007**, *99*, 4.
[261] K. Zhao, T. G. Mason, *Phys. Rev. Lett.* **2007**, *99*, 268301.
[262] S. Asakura, F. Oosawa, *J. Polym. Sci.* **1958**, *33*, 183–192.
[263] P. D. Kaplan, J. L. Rouke, A. G. Yodh, D. J. Pine, *Phys. Rev. Lett.* **1994**, *72*, 582–585.
[264] L. Onsager, *Ann. NY Acad. Sci.* **1949**, 627.
[265] K. H. Lin, J. C. Crocker, V. Prasad, A. Schofield, D. A. Weitz, T. C. Lubensky, A. G. Yodh, *Phys. Rev. Lett.* **2000**, *85*, 1770–1773.
[266] G. Odriozola, F. Jimenez-Angeles, M. Lozada-Cassou, *J. Chem. Phys.* **2008**, *129*, 4.
[267] B. J. Alder, T. E. Wainwright, *J. Chem. Phys.* **1957**, *27*, 1208–1209.
[268] H. Reiss, A. D. Hammerich, **1986**, *90*, 6252–6260.
[269] Z. D. Cheng, W. B. Russell, P. M. Chaikin, *Nature* **1999**, *401*, 893–895.
[270] S. Fraden, G. Maret, D. L. D. Caspar, R. B. Meyer, *Phys. Rev. Lett.* **1989**, *63*, 2068–2071.
[271] M. D. Rintoul, S. Torquato, *J. Chem. Phys.* **1996**, *105*, 9258–9265.
[272] F. H. Stillinger, P. G. Debenedetti, S. Chatterjee, *J. Chem. Phys.* **2006**, *125*, 11.
[273] C. Bechinger, *Curr. Opin. Colloid Interface Sci.* **2002**, *7*, 204–209.
[274] P. Bartlett, A. I. Campbell, *Phys. Rev. Lett.* **2005**, *95*, 4.
[275] E. V. Shevchenko, D. V. Talapin, C. B. Murray, S. O'Brien, *J. Am. Chem. Soc.* **2006**, *128*, 3620–3637.
[276] W. Gotze, *J. Phys. Condensed Matt.* **1998**, *11*, A1–A45.
[277] Z. Dogic, S. Fraden, *Curr. Opin. Colloid Interface Sci.* **2006**, *11*, 47–55.

Received: March 1, 2009
Published online: June 10, 2009

